UC San Diego
UC San Diego Previously Published Works

Title

Underwater Image Restoration Based on Image Blurriness and Light Absorption

Permalink

Journal

ISSN

Authors

Peng, Yan-Tsung
Cosman, Pamela C

Publication Date

DOI

Peer reviewed

Underwater Image Restoration Based on Image Blurriness and Light Absorption

Yan-Tsung Peng, *Student Member, IEEE*, and Pamela C. Cosman, *Fellow, IEEE*

Abstract—Underwater images often suffer from color distortion and low contrast, because light is scattered and absorbed when traveling through water. Such images with different color tones can be shot in various lighting conditions, making restoration and enhancement difficult. We propose a depth estimation method for underwater scenes based on image blurriness and light absorption, which can be used in the image formation model (IFM) to restore and enhance underwater images. Previous IFM-based image restoration methods estimate scene depth based on the dark channel prior or the maximum intensity prior. These are frequently invalidated by the lighting conditions in underwater images, leading to poor restoration results. The proposed method estimates underwater scene depth more accurately. Experimental results on restoring real and synthesized underwater images demonstrate that the proposed method outperforms other IFM-based underwater image restoration methods.

Index Terms—Underwater image, image restoration, image enhancement, depth estimation, blurriness, light absorption.

I. INTRODUCTION

TECHNOLOGY advances in manned and remotely operated submersibles allow people to collect images and videos from a wide range of the undersea world. Waterproof cameras have become popular, allowing people to easily record underwater creatures while snorkeling and diving. These images or videos often suffer from color distortion and low contrast due to the propagated light attenuation with distance from the camera, primarily resulting from absorption and scattering effects. Therefore, it is desirable to develop an effective method to restore color and enhance contrast for these images.

Even though there are many image enhancing techniques developed, such as white balance, color correction, histogram equalization, and fusion-based methods [1], they are not based on a physical model underwater, and thus are not applicable for underwater images with different physical properties. It is challenging to restore underwater images because of the variation of physical properties. Light attenuation underwater leads to different degrees of color change, depending on wavelength, dissolved organic compounds, water salinity, and concentration of phytoplankton [2]. In water, red light with a longer

The authors are with the Department of Electrical and Computer Engineering, University of California at San Diego, La Jolla, CA 92093, USA (e-mail: yapeng@ucsd.edu; pcosman@ucsd.edu).

Color versions of one or more of the figures in this paper are available online at http://ieeexplore.ieee.org.
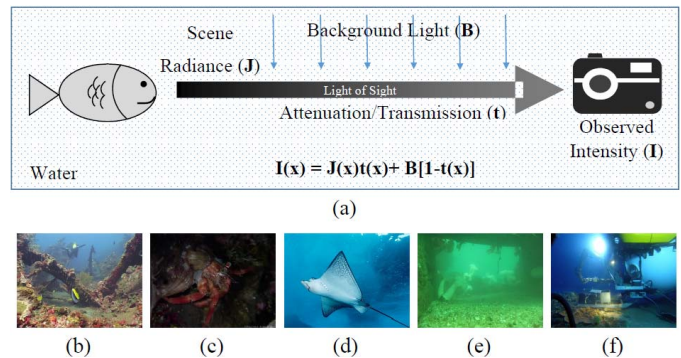
Fig. 1. (a) Simplified image formation model. (b)–(f) Examples of underwater images having different underwater color tones. The original images (b) and (c) are from [35], (d) from www.webmastergrade.com, (e) from scuba-diving.knoji.com/amazing-underwater-parks and (f) from [36].

wavelength is absorbed more than green and blue light. Also, scattered background light coming from different colors of water is blended with the scene radiance along the light of sight [3], resulting in underwater scenes often having low contrast and color distortions.

Fig. 1(a) depicts a simplified image formation model (IFM) [4]–[6] to describe an underwater scene. Here $I(x)$, the observed intensity at pixel x, consists of the scene radiance $J(x)$ blended with the background light (BL) B according to the transmission map (TM) $t(x)$. The TM describes the portion of the scene radiance that is not scattered or absorbed and reaches the camera. Therefore, a closer scene point has a larger value in the TM. Fig. 1(b)-(f) shows five underwater images with different BL.

In order to restore color and enhance contrast for such images, several attempts have been made using the IFM [8]–[17], where scene depth is derived from the TM [7]. In [8], [10], [11], and [15], the TM is derived by the dark channel prior (DCP) [7], which was first proposed to remove haze in natural terrestrial images by calculating the amount of spatially homogeneous haze using the darkest channel in the scene. It was observed that because points in the scene closer to the camera have a shorter path over which scattering occurs, close dark scene points would remain dark as they would experience less brightening from scattered light. Thus, the DCP can be used to estimate the TM and scene depth. However, red light that possesses longer wavelength and lower frequency attenuates faster underwater. Thus the DCP based on RGB channels (DCP_{rgb}) in an underwater scene would often end up considering only the red channel to measure transmission, leading to erroneous depth estimation and poor

restoration results. In [12], [13], and [17], an underwater DCP based on only the green and blue channels (DCP$_{gb}$) was proposed to avoid this problem. Similarly, Galdran *et al.* [14] proposed the Red Channel method, whose DCP is based on green, blue, and inverted red channels (DCP$_{r'gb}$). Instead of using the DCP, Carlevaris-Bianco *et al.* [9] adopted the maximum intensity prior (MIP) that uses the difference between the maximum intensity of the red channel and that of the green and blue channels to estimate the TM. However, these methods frequently perform poorly because the light absorption and different lighting conditions existing in underwater images make many exceptions to those priors. Moreover, no work has been done on restoration of underwater images with dim BL, which frequently violate the assumptions underlying the DCPs and the MIP. For example, the DCPs or the MIP of dark background pixels would have small values and therefore be mistakenly judged as being close to the camera.

To improve DCP- or MIP-based methods, our previous work [16] uses image blurriness to estimate transmission and scene depth, because larger scene depth causes more object blurriness for underwater images. The method can properly restore those underwater images that make exceptions to the DCP- or MIP-based methods because it does not estimate underwater scene depth via color channels. In this paper, we improve our previous work. The specific improvements relative to [16] are as follows: (a) Rather than estimating depth using image blurriness alone, we use both image blurriness and light absorption. While blurriness is an important indicator of depth, it is not the only cue underwater, and the differential absorption of red light can be exploited when the red content is significant. (b) We improve on the estimation of BL, in that we determine BL from candidate BLs estimated from blurry regions. (c) We present the most comprehensive comparison to date of underwater image restoration techniques, using no-reference quality assessment tools (BRISQUE [18], UIQM [19], and UCIQE [20]), as well as two full-reference approaches (PSNR and SSIM [21]) based on synthesized underwater images with scaled and shifted known depth maps.

The rest of the paper is organized as follows. In Section II, we review underwater image restoration methods based on the IFM. The proposed method is described in Section III. Qualitative and quantitative experimental results are reported in Section IV. Section V combines the proposed method with histogram equalization and compares against an underwater image enhancement method. Finally, Section VI summarizes the conclusions.

II. RELATED WORK

A. Underwater Image Restoration Based on DCP/MIP

The simplified IFM [4]–[6] is given as:

$$I^c(x) = J^c(x)t^c(x) + B^c\big(1 - t^c(x)\big), c \in \{r, g, b\} \quad (1)$$

where $I^c(x)$ is the observed intensity in color channel c of the input image at pixel x, J^c is the scene radiance, B^c is the BL, and t^c is the TM, where c is one of the red, green, and blue channels. Note that I^c and J^c are normalized to the range between 0 and 1 in this paper. The TM t^c is commonly

written as an exponential decay term [7], [14], [15] based on the Beer-Lambert law [22] of light attenuation:

$$t^c(x) = e^{-\beta^c d(x)}, \quad (2)$$

where $d(x)$ is the distance from the camera to the radiant object and β^c is the spectral volume attenuation coefficient for channel c, where c is one of the red, green, and blue channels.

To estimate B^c and t^c, the DCP finds the minimum value among three color channels in a local patch of an image [7]. The DCP for a hazy image can be computed as:

$$I_{dark}^{rgb}(x) = \min_{y \in \Omega(x)} \left\{ \min_{c \in \{r,g,b\}} I^c(y) \right\}, \quad (3)$$

where $\Omega(x)$ is a square local patch centered at x. For an outdoor scene with haze, the value of the dark channel of a farther scene point in the input image is in general larger than for a closer scene point because of scattered light.

To determine BL B^c, the top 0.1% brightest pixels in I_{dark}^{rgb} were picked in [7]. Let $p_{0.1\%}$ be the set of positions of those bright pixels in I_{dark}^{rgb}. Then, among these pixels, the one corresponding with the highest intensity in the input image I^c is chosen to provide the estimate of BL. The estimated BL $\widetilde{B^c}$ can be described as:

$$\widetilde{B^c} = I^c \bigg(\arg\max_{x \in p_{0.1\%}} \sum_{c \in \{r,g,b\}} I^c(x) \bigg). \quad (4)$$

There are several variants of BL estimation methods listed in Table I.

For a haze-free image, $t^c = 1$ in Eq. (1), so $I^c = J^c$. For an outdoor terrestrial haze-free image, J_{dark}^{rgb} usually equals zero, because for most pixels x, at least one of three color channels will have a low-intensity pixel in the local patch $\Omega(x)$ around x. This is not true for bright sky pixels, where nearby pixels also tend to be bright. Thus, it asserts in [7, eq. (9)] that

$$J_{dark}^{rgb}(x) = \min_{y \in \Omega(x)} \left\{ \min_{c \in \{r,g,b\}} J^c(y) \right\} = 0, \quad (5)$$

for about 75% of non-sky pixels in haze-free images.

To estimate t^c, dividing both sides of Eq. (1) by B^c and then applying the minimum operators to it, we obtain

$$\min_{y \in \Omega(x)} \left\{ \min_c \frac{I^c(y)}{B^c} \right\} = \min_{y \in \Omega(x)} \left\{ \min_c \frac{J^c(y)}{B^c} t^c(y) \right\} + 1 - \tilde{t}(x), \quad (6)$$

where the estimated TM $\tilde{t}(x) = \min_{y \in \Omega(x)} \{\min_c t^c(y)\}$. Since $\min_{y \in \Omega(x)} \left\{ \min_c \frac{J^c(y)}{B^c} t^c(y) \right\} = 0$ based on Eq. (5), $\tilde{t}$ is estimated by:

$$\tilde{t}(x) = 1 - \min_{y \in \Omega(x)} \left\{ \min_{c \in \{r,g,b\}} \frac{I^c(y)}{B^c} \right\}, \quad (7)$$

where $\tilde{t}(x)$ is clipped to zero if negative.

The TM estimation described in Eq. (7) is a general approach to measuring scene transmission, useful to recover the scene radiance J^c using Eq. (1). It is based on three assumptions for hazy terrestrial images: overcast lighting, spatially invariant attenuation coefficients, and wavelength-independent attenuation $\beta^r = \beta^g = \beta^b = \beta$,

TABLE I

FORMULAS FOR ESTIMATION OF DEPTH, BL, AND TM IN UNDERWATER IMAGE RESTORATION METHODS [8]–[16]

Method	Prior (p) on I^c	BL estimation ($\widetilde{B^c}$)	TM estimation ($\tilde{t}$ or $\widetilde{t^c}$)
[8]	I^{rgb}_{dark}	$I^c\big(\arg\max_x p(x)\big)$	$\tilde{t}(x) = 1 - \min_k\big(\min_{y\in\Omega(x)} I^k(y)\widetilde{B^k}\big)$
[9]	D_{mip}	$I^c\big(\arg\min_x \tilde{t}(x)\big)$	$\tilde{t}(x) = D_{mip}(x) + \big(1 - \max_x D_{mip}(x)\big)$
[10]	I^{rgb}_{dark}	$I^c\big(\arg\max_{x\in p_{0.1\%}}(\sum_k I^k(x))\big)$	$\tilde{t}(x) = 1 - \min_k\big(\text{med}_{y\in\Omega(x)}\frac{I^k(y)}{\widetilde{B^k}}\big)$
[11]	I^{rgb}_{dark}	$I^c\big(\arg\max_x I^c_{dark}(x)\big)$	$\widetilde{t^r}(x) = 1 - \min_k\big(\min_{y\in\Omega(x)}\frac{I^k(y)}{\widetilde{B^k}}\big),\ \widetilde{t^{c'}} = (\widetilde{t^r})^{\frac{\beta^{c'}}{\beta^r}}$
[12]	I^{gb}_{dark}	$I^c\Big(\arg\min_x\big(I^r_{dark}(x) - \max_{k'}(I^{k'}_{dark}(x))\big)\Big)$	$\widetilde{t^{c'}}(x) = 1 - \min_{k'}\big(\min_{y\in\Omega(x)}\frac{I^{k'}(y)}{\widetilde{B^{k'}}}\big),$ $\widetilde{t^r} = (\tau\max_{y\in\Omega(x)} I^r(y)),\ \tau = \frac{\text{avg}_x(\widetilde{t^{c'}}(x))}{\text{avg}_x\big(\max_{y\in\Omega(x)} I^r(y)\big)}$
[13]	I^{gb}_{dark}	$I^c\big(\arg\max_x p(x)\big)$	$\tilde{t}(x) = 1 - \min_k\big(\min_{y\in\Omega(x)}\frac{I^k(y)}{\widetilde{B^k}}\big)$
[14]	$I^{r'gb}_{dark}$	$I^c\big(\arg\min_{x\in p_{10\%}} I^r(x)\big)$	$\tilde{t}(x) = 1 - \min\Big(\frac{\min_{y\in\Omega(x)}(1-I^r(y))}{1-\widetilde{B^r}},$ $\frac{\min_{y\in\Omega(x)} I^g(y)}{\widetilde{B^g}}, \frac{\min_{y\in\Omega(x)} I^b(y)}{\widetilde{B^b}}\Big)$
[15]	I^{rgb}_{dark}	$I^c\Big(\arg\max_{x\in p_{0.1\%},c'}\big|I^r(x) - I^{c'}(x)\big|\Big)$	$\widetilde{t^r}(x) = 1 - \min_k\big(\min_{y\in\Omega(x)}\frac{I^k(y)}{\widetilde{B^k}}\big),\ \widetilde{t^{c'}} = (\widetilde{t^r})^{\frac{\beta^{c'}}{\beta^r}}$
[16]	$1 - P_{blr}$	$\frac{1}{|p_{0.1\%}|}\sum_{x\in p_{0.1\%}} I^c(x)$	$\tilde{t}(x) = F_s\big(P_{blr}(x)\big)^\dagger$

$c, k \in \{r,g,b\};\ c', k' \in \{g,b\};$
$^\dagger F_s$ is described in Eq. (20).

i.e., $\widetilde{t^r} = \widetilde{t^g} = \widetilde{t^b} = \tilde{t}$ [5]. Table I also lists several TM estimation methods based on Eq. (7) which have been modified for underwater scenes.

Since the estimated TM has block-like artifacts, it can be refined by either soft matting [24] or guided filtering [25]. With the estimated $\tilde{t}$ and a given β, the estimated depth map can be calculated according to Eq. (2).

Finally, by putting I^c, $\widetilde{t^c}$ and $\widetilde{B^c}$ into Eq. (1), the estimated scene radiance is calculated as $\tilde{J}^c = (I^c - \widetilde{B^c})/\widetilde{t^c} + \widetilde{B^c}$. In order to increase the exposure of the scene radiance for display, a lower bound t_0 for $\widetilde{t^c}$, empirically set to 0.1, is incorporated as:

$$\tilde{J}^c(x) = \frac{I^c(x) - \widetilde{B^c}}{\max(\widetilde{t^c}(x), t_0)} + \widetilde{B^c}, \tag{8}$$

Basically, this restoration step is adopted in [9]–[16] with an extra smoothing step for [9], an additional color correction method for [10], a color compensation method for [11], and a color correction weighting factor incorporated in Eq. (8) for [14].

The MIP, another prior to estimate the TM, was proposed in [9]. It first calculates the difference between the maximum intensity of the red channel and that of the green and blue channels as:

$$D_{mip}(x) = \max_{y\in\Omega(x)} I^r(y) - \max_{y\in\Omega(x)}\{I^g(y), I^b(y)\}. \tag{9}$$

Large values of $D_{mip}(x)$ represent closer scene points whose red light attenuates less than that of farther scene points. Then the TM is estimated by $\tilde{t}(x) = D_{mip}(x) + (1 - \max_x D_{mip}(x))$. Table I summarizes all the priors, and BL and TM estimation methods in [8]–[16].
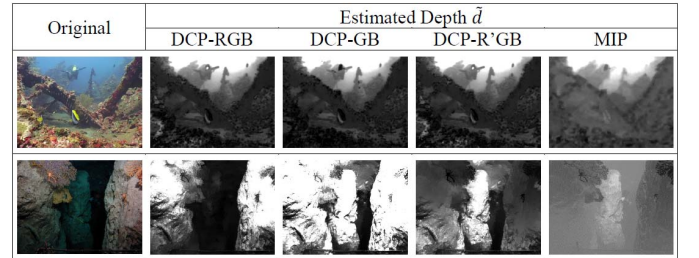

Original	Estimated Depth $\tilde{d}$			
	DCP-RGB	DCP-GB	DCP-R'GB	MIP

Fig. 2. Examples of depth estimation via the DCP$_{rgb}$, DCP$_{gb}$, DCP$_{r'gb}$ and MIP for underwater images. The first row of images shows a successful case with BL (0.42, 0.68, 0.86). The second row shows a failure case with BL (0.04, 0.07, 0.07). The original images for the first and second rows come from [35] and [36].

These DCP- and MIP-based methods only work in limited cases. Underwater images have different possible lighting conditions, which may violate the assumptions underlying these priors, leading to poor estimation and restoration results. In the original image in the first row of Fig. 2, the lighting conditions are appropriate for these methods. The foreground fish and rock have dark pixels which cause the dark channel to have a small value, so they are correctly estimated as being close. By contrast, the background lacks very dark pixels, so the dark channel has a larger value, and these regions are correctly estimated to be relatively far away. For the MIP, the value of D_{mip} of a closer scene point is larger than that of a farther scene point, which can also be properly interpreted as the scene depth.

The image in the second row of Fig. 2 is an example of an underwater image shot with artificial lights where both the DCP and MIP work poorly. The bright foreground pixels are mistakenly judged to be far based on the DCPs. The dark
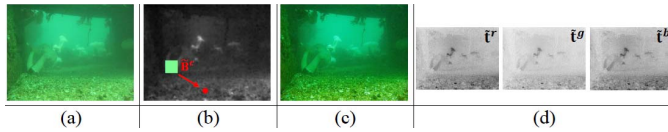
Fig. 3. An example of inaccurate TM and BL estimation causing an unsatisfying restoration result. (a) Original image, (b) depth map, and estimated BL $\widetilde{B^c}$ picked at the position of the red dot, (c) recovered scene radiance obtained using [15], and (d) estimated TMs for the red, green, and blue channels.

background region is incorrectly regarded as being close. The MIP also produces an erroneous depth map because the values of D_{mip} for the whole image are very similar. Note that since correct depth estimation requires both the BL and TM of an underwater image to be correctly estimated in Fig. 2, we compare the depth maps obtained using different priors with fixed and properly selected BLs. Later in Section IV, we will show other examples where the DCP and the MIP poorly estimate depth and BL, leading to unsatisfying restoration results.

B. TM Estimation for the Red, Green, and Blue Channels

As described previously, underwater image restoration methods that require the three assumptions often fail to recover scene radiance underwater because imaging conditions are quite different than in open air. The natural illumination undergoes a strong color-dependent attenuation, which violates the assumption of wavelength-independent attenuation $\beta^r = \beta^g = \beta^b$.

Chiang *et al.* [11] first addressed this problem by proposing a wavelength compensation and image dehazing method. In this, the TMs are estimated according to residual energy ratios of different color channels, related to the attenuation coefficients β^c. However, these ratios were chosen manually, limiting the practical applicability of this method.

In [15], the relations among the attenuation coefficients of different color channels based on inherent optical properties of water were derived from the BL as:

$$\frac{\beta^k}{\beta^r} = \frac{B^r(m\lambda^k + i)}{B^k(m\lambda^r + i)}, k \in \{g, b\}, \qquad (10)$$

where $\lambda^c, c \in \{r, g, b\}$, represent the wavelengths of the red, green, and blue channels, $m = -0.00113$, and $i = 1.62517$. The TMs for the green and blue lights are then calculated by:

$$t^k(x) = t^r(x)^{\frac{\beta^k}{\beta^r}}, k \in \{g, b\}, \qquad (11)$$

where t^r is estimated by Eq. (7).

As described above, correct TM estimation is contingent on the prior and BL it uses. Both of these frequently cannot be attained in [11] and [15] because the prior they use is the DCP$_{rgb}$. Fig. 3 shows an example of an incorrect TM and BL obtained using DCP$_{rgb}$ in [15] producing a poor restoration result. Here, the original image has some bright foreground pixels and some dark background pixels. Thus, instead of picking BL from the bright background pixels, the method selects BL from foreground pixels erroneously regarded as being far. Moreover, wrong BL causes the TMs, $\widetilde{t^r}$, $\widetilde{t^g}$, and $\widetilde{t^b}$, to be similar to each other for this greenish input image, thus failing to correct the distorted color.
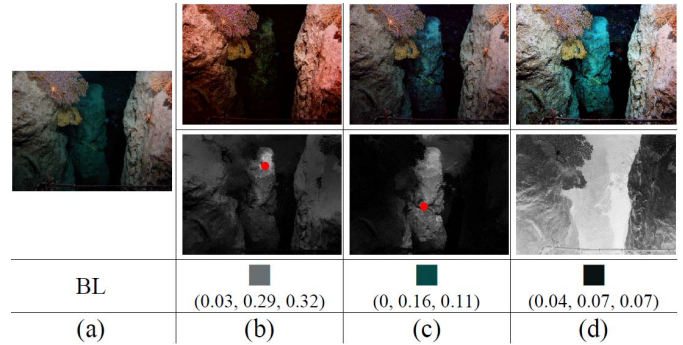

Fig. 4. Example of restoring an underwater image with artificial lighting using [14] and the proposed method. (a) The original image. The restoration results and their corresponding depth maps and BL (marked with a red dot) obtained using (b) [14] based on the DCP$_{r'gb}$, (c) [14] based on the DCP$_{r'gb}$ with saturation, and (d) more accurate TMs and properly selected BL. The original image is from [36].

C. DCP/MIP Exceptions Caused by Artificial Illumination

Since water absorbs more light as the light rays travel through longer distance in the water, artificial lighting is sometimes used to provide sufficient light for taking pictures and videos. Artificial lighting in an underwater image often leads to a bright foreground. This violates the assumptions underlying the DCP, where bright pixels are regarded as being far. Artificially illuminated bright foreground pixels should be less modified by a restoration method than background pixels because the light, originating from an artificial lighting source and reflected by foreground objects, travels less far in the water and is less absorbed and scattered. Depth estimation based on the MIP could fail when the foreground has bright pixels and the background has dark pixels because the values of D_{mip} for the foreground and the background would be similar, which is unable to produce an accurate depth map. An example of the failure of DCP and MIP to estimate scene depth is shown in the second row of Fig. 2. We will demonstrate more examples in Sec. IV.

Chiang *et al.* [11] proposed to detect and then remove artificial lighting by comparing the mean luminances of the foreground and the background. However, this approach classifies foreground and background pixels based on the depth map using DCP, which is often ineffective because of incorrect depth estimation.

Galdran *et al.* [14] dealt with artificial lighting by incorporating the saturation prior into DCP$_{r'gb}$ as:

$$I_{dark}^{r'gb-sat}(x) = \min_{y \in \Omega(x)} \left\{ \min_{c \in \{r', g, b\}} I^c(y), Sat(y) \right\}, \qquad (12)$$

where $Sat = \frac{\max_c(I^c) - \min_c(I^c)}{\max_c(I^c)}$, $c \in \{r, g, b\}$ measures the saturation of scene point y. Because it is assumed that artificially illuminated scene points would have low saturation, these bright points in the foreground would not be incorrectly judged as being far. However, it does not solve the problem caused by dark pixels in the background, which still violate the assumptions underlying the DCP. As shown in Fig. 4(b), restoration based on DCP$_{r'gb}$ estimates the scene depth incorrectly, as the rock in the foreground has bright pixels because of artificial lighting, so is wrongly judged to be far. In Fig. 4(c), depth
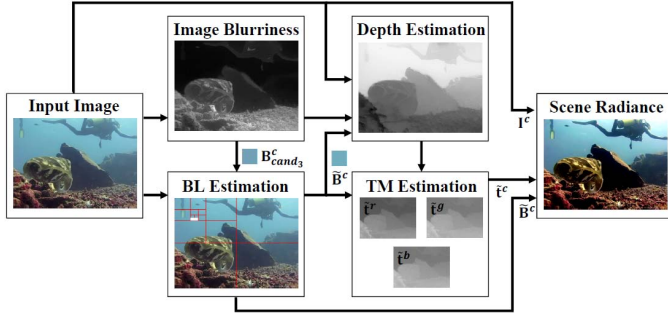
Fig. 5. Flowchart of our proposed method. The original image is from [35].
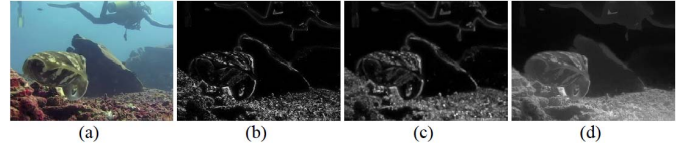

Fig. 6. Example of image blurriness estimation. (a) Original image, (b) Initial blurriness map from Eq. (13), (c) Rough map from Eq. (14), (d) Refined map from Eq. (15).
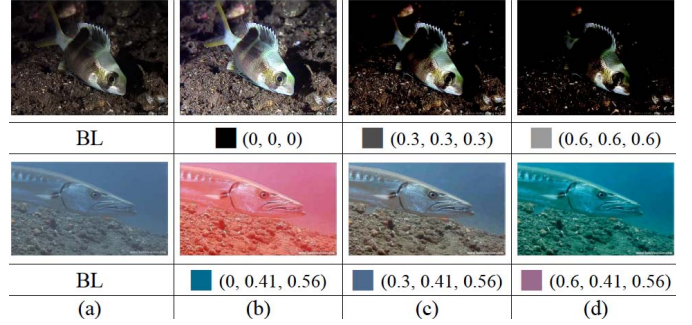

Fig. 7. Examples of changing brightness or hue of restored scene radiance via varying BL with given TMs obtained using the proposed method. (a) Original images. (b), (c), and (d) are the restored images using different BL. The original images are from [35].

estimation based on the $DCP_{r,gb}$ with saturation successfully avoids this problem, but the dark pixels in the background are still erroneously estimated to be close, also resulting in an incorrect BL selection and poor restoration result. With more accurate TMs and properly selected BL, Fig. 4(d) shows a better restoration result image.

III. PROPOSED METHOD

In this section, we propose a new restoration method based on both image blurriness and light absorption, where more accurate BL and depth estimation are provided. First, we select the BL from blurry regions in an underwater image. Then, based on the BL, the depth map and the TMs are obtained to restore scene radiance. The flowchart of the proposed method is shown in Fig. 5.

A. Image Blurriness Estimation

Underwater image blurriness estimation was presented in our previous work [16]. It includes three steps. Let $G^{k,\sigma}$ be the input image filtered by a $k \times k$ spatial Gaussian filter with variance σ^2. The initial blurriness map P_{init} is computed as:

$$P_{init}(x) = \frac{1}{n}\sum_{i=1}^{n}|I_g(x) - G^{r_i,r_i}(x)|, \qquad (13)$$

where I_g is the grayscale version of the input image I^c, $r_i = 2^i n + 1$, and n is set to 4. Next, we apply the max filter to calculate the rough blurriness map P_r as:

$$P_r(x) = \max_{y \in \Omega(x)} P_{init}(y), \qquad (14)$$

where $\Omega(x)$ is a $z \times z$ local patch centered at x. Here, we set $z = 7$. (We found that any patch size from $z = 7$ up to $z = 31$ works well for image sizes ranging from 800x600 to 1280x720 in the proposed method. So $z = 7$ is used throughout this paper.) We refine P_r by filling the holes caused by flat regions in the objects using morphological reconstruction [23], and then soft matting [24] or guided filtering [25] is applied for smoothing to generate a refined blurriness map P_{blr}:

$$P_{blr}(x) = F_g\left\{C_r\left[P_r(x)\right]\right\}, \qquad (15)$$

where C_r is a hole-filling morphological reconstruction operator, and F_g is the soft matting or guided filtering function. Fig. 6 shows an example of each step.

B. Background Light Estimation

BL determines the color tone of an underwater image as well as its restored scene radiance. For an underwater image, the lower and upper bounds of its possible restored scene radiance $\widetilde{J^c} \in [0, 1]$ can be derived by setting $\widehat{B^c} = 1$ and $\widehat{B^c} = 0$ in Eq. (8), as:

$$\max\left(\frac{I^c - 1 + \tilde{t}'}{\tilde{t}'}, 0\right) \leq \widetilde{J^c} \leq \min\left(\frac{I^c}{\tilde{t}'}, 1\right), \qquad (16)$$

where $\tilde{t}' = \max(\tilde{t}^c, t_0) \in [t_0, 1]$. Based on Eq. (16), restoring an underwater image with dim BL would result in bright scene radiance while using bright BL leads to an opposite result. Consider an extreme BL, $\widehat{B^c} = 0$, as an example, where $\widetilde{J^c} = \min(\frac{I^c}{\tilde{t}'}, 1)$. In this case, the restored scene radiance $\widetilde{J^c}(x)$ of a far scene point with the value of $\tilde{t}'(x)$ being small would have a larger value than its corresponding observed intensity $I^c(x)$ and thus be brighter. A bright BL would lead to the opposite result. A visual example can be seen in the first row of Fig. 7. As the BL, though unchanging, is estimated as being brighter, the restored scene radiance gets darker. Moreover, a small value in one of the color channels of the estimated BL will lead to a substantial increase in that color in the restored image. The second row of Fig. 7 gives an example in which changing values in the red channel of $\widehat{B^c}$ produces different hues of the restored images.

In general, the value for estimated BL of an underwater image is chosen from far scene points with high intensity. Emberton *et al.* [17] adopted a hierarchical rank-based approach based on DCP_{gb}, color variance, and gradient to find the brightest pixel in the most likely region of BL. This method is, however, inaccurate in many cases, as it still uses the assumptions of DCP_{gb}. In contrast, we estimate the BL based on image blurriness and variance. We propose a BL candidate

---

Algorithm 1 BL–Estimate

1: Input parameter: input image I^c, blurriness map P_{blr}.
2: Output parameter: estimated BL $\widetilde{B^c}$.
3:
4: **function** BL–ESTIMATE(I^c, P_{blr})
5:      $B^c_{cand_1} \leftarrow \text{avg}_x \left[\text{QUAD–SELECT–LV}(I^c) \right]$;
6:      $B^c_{cand_2} \leftarrow \text{avg}_x \left[\text{QUAD–SELECT–LB}(I^c, P_{blr}) \right]$;
7:      $B^c_{cand_3} \leftarrow \frac{1}{|P_{0.1\%}|} \sum_{x \in P_{0.1\%}} I^c(x)$;
8:      $B^c_{max} \leftarrow \max_{i \in \{1,2,3\}} B^c_{cand_i}$;
9:      $B^c_{min} \leftarrow \min_{i \in \{1,2,3\}} B^c_{cand_i}$;
10:      **for** $k \in \{r, g, b\}$ **do**
11:          $\alpha \leftarrow S(\frac{|I^k > 0.5|}{\textbf{Size}(I^k)}, \epsilon_n)$;
12:          $\widetilde{B^k} \leftarrow \alpha B^k_{max} + (1 - \alpha) B^k_{min}$;
13:      **end for**
14:      **return** $\widetilde{B^c}$;
15: **end function**
16:
17: **function** QUAD–SELECT–LB(I^c, P_{blr})
18:      $I_{gray} \leftarrow$ **rgb2gray**(I);
19:      $I_q \leftarrow I_{gray}$;
20:      **while** $\frac{\textbf{Size}(I_q)}{\textbf{Size}(I_{gray})} > \epsilon_s$ **do**
21:          Partition I_q into four quadrants, I_q^1, I_q^2, I_q^3, and I_q^4;
22:          Pick I_q^n with largest blurriness computed using P_{blr};
23:          $I_q \leftarrow I_q^n$;
24:      **end while**
25:      **return** $I^c(\textbf{Position}(I_q))$;
26: **end function**

---

selection method, which picks three BL candidates from the top 0.1% blurry pixels in the input image, the lowest variance region and the largest blurriness region. These two regions (which may or may not be the same) are decided using quadtree decomposition which iteratively divides the input image into four equal-sized blocks according to the variance or blurriness. The blurriness of a region in the input image is obtained by averaging $P_{blr}(x)$ in the corresponding region in the blurriness map.

With three BL candidates determined, we pick BL for each color channel separately from them according to the input image. The detailed algorithm is described in Algo. 1, where S is a sigmoid function given by:

$$S(a, v) = \left[1 + e^{-s(a-v)} \right]^{-1}, \qquad (17)$$

where s is an empirical constant. Here, we set $s = 32$. The fixed thresholds used in this paper are $\epsilon_s = 2^{-10}$ and $\epsilon_n = 0.2$. Note that the function QUAD–SELECT–LV is a similar function to QUAD–SELECT–LB with largest blurriness being replaced by lowest variance and without considering P_{blr}.

In BL–ESTIMATE, we determine BL for each color channel between the darkest and brightest BL candidates according to the percentage of bright pixels ($I^k > 0.5$). When the percentage is high ($\frac{|I^k > 0.5|}{\text{Size}(I^k)} >> \epsilon_n$), meaning that the input image was taken under sufficient lighting, then BL estimated as being brighter is more suitable. When the image was taken

without sufficient lighting ($\frac{|I^k > 0.5|}{\text{Size}(I^k)} << \epsilon_n$), BL is estimated as being darker. In between these extremes, the BL estimate is calculated by a weighted combination of the darkest and brightest BL candidates. Fig. 8 demonstrates the proposed BL estimation and compares the restoration results obtained using each BL candidate and the selected estimated BL, where we can see that using our background light candidate selection method generates a more visually pleasing result.

C. Depth Estimation Based on Light Absorption and Image Blurriness

We propose to estimate scene depth by combining three depth estimation methods. We first define the three depth estimation methods, and then explain how they are sigmoidally combined based on the lighting and image conditions where each performs best.

The red channel map R is defined as:

$$R(x) = \max_{y \in \Omega(x)} I^r(y). \qquad (18)$$

We obtain a first estimate of depth, denoted $\widetilde{d_R}$, directly from the red channel map by assuming that scene points which preserve more red light are closer to the camera:

$$\widetilde{d_R} = 1 - F_s(R), \qquad (19)$$

where F_s is a stretching function:

$$F_s(\mathbf{V}) = \frac{\mathbf{V} - \min(\mathbf{V})}{\max(\mathbf{V}) - \min(\mathbf{V})}, \qquad (20)$$

where $\mathbf{V}$ is a vector. Some successful examples are shown in Fig. 9(a)–(d).

Our second estimate of depth is

$$\widetilde{d_D} = 1 - F_s(D_{mip}), \qquad (21)$$

which uses Eq. (9) and (20). This depth map assumes that, for a scene point, a greater value of red light minus the maximum of green and blue lights means the point is closer to the camera. This concept was first proposed in [9], where D_{mip} was used to estimate the TM, rather than the depth directly.

Our third approach is to use the image blurriness P_r in Eq. (14) to estimate depth:

$$\widetilde{d_B} = 1 - F_s(C_r(P_r)). \qquad (22)$$

Combining Eq. (19), Eq. (21), and Eq. (22), we propose to estimate underwater scene depth based on light absorption and image blurriness according to the estimated BL $\widetilde{B^c}$ and the average input red value:

$$\widetilde{d_n}(x) = \theta_b \left[\theta_a \widetilde{d_D}(x) + (1 - \theta_a) \widetilde{d_R}(x) \right] + (1 - \theta_b) \widetilde{d_B}(x), \qquad (23)$$

where $\theta_a = S(\text{avg}_c(\widetilde{B^c}), 0.5)$ and $\theta_b = S(\text{avg}(I^r), 0.1)$ are determined by the sigmoid function defined in Eq. (17). Finally, the depth map is refined and smoothed by either soft matting [24] or guided filtering [25]. The estimated depth map $\widetilde{d_n} \in [0, 1]$ can be regarded as a map of normalized relative distance for the scene points of the input image.
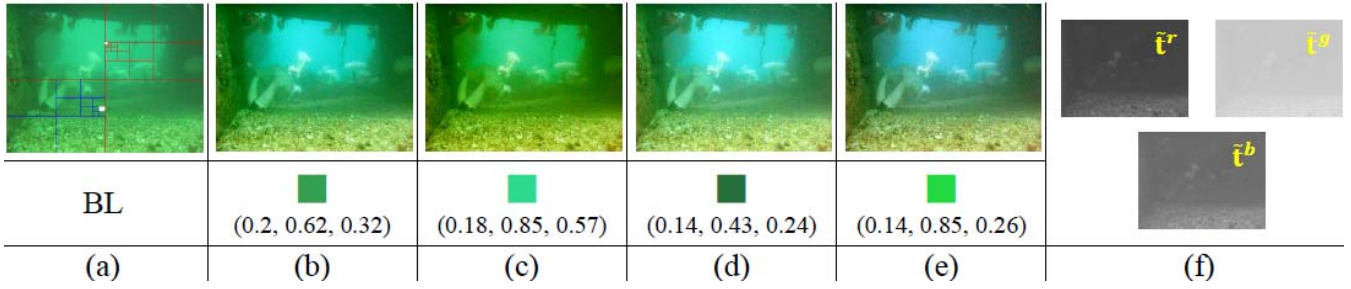
Fig. 8.   Example of the proposed BL estimation. (a) The original image with the lowest variance and largest blurriness estimation blocks outlined in red and in blue. The white blocks are the final quadrants. The images (b)–(e) are the restored images obtained using $B^c_{cand_1}$, $B^c_{cand_2}$, $B^c_{cand_3}$, and $\widetilde{B^c}$. (f) The TMs for the red, green and blue channels estimated by the proposed method with $\widetilde{B^c}$.
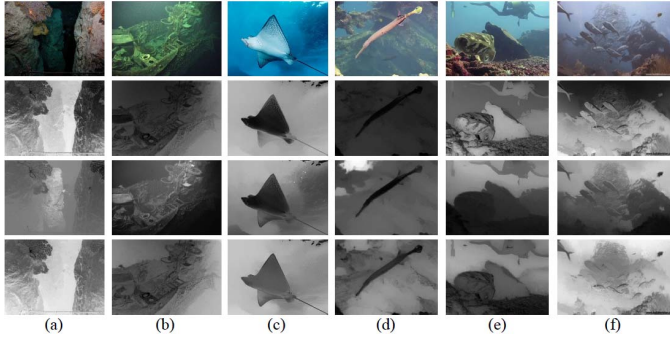

Fig. 9.   Examples of depth estimation based on light absorption and image blurriness. The original images are in the first row. The depth maps obtained based on the red channel R, D_{mip}, and P_{blr} are in the second, third, and fourth rows. The means of the estimated BL $\text{avg}_{c\in\{r,g,b\}}(\widetilde{B^c})$ in the column (a)–(f) are 0.06, 0.18, 0.5, 0.53, 0.62, and 0.81. The original image (b) is from [36], and (d)–(f) are from [35].

The explanation for this combined approach is as follows. When the image has some reasonable level of red content overall ($\text{avg}(I^r) >> 0.1$) and the background light is relatively dim ($\text{avg}_c(\widetilde{B^c}) << 0.5$) then $\widetilde{d_R}$ alone represents depth well. In this case, $\theta_a \approx 1$ and $\theta_b \approx 1$, and $\widetilde{d_n}(x) \approx \widetilde{d_R}(x)$. As the BL gets brighter, the possibility that $\widetilde{d_R}(x)$ fails to represent scene depth gets higher. Because the BL accounts for more of the observed intensity for a scene point farther from the camera, far scene points may still have large values in the red channel and be wrongly judged as being close according to Eq. (19), as seen in Fig. 9 (e)–(f).

When an underwater image has a brighter BL, we find that $\widetilde{d_D}$ is more reliable to represent scene depth. The red light of a farther scene point is absorbed more compared to the green and blue light, shown in Fig. 9 (c)–(f). So when the image has some reasonable level of red content overall ($\text{avg}(I^r) >> 0.1$) and the background light is relatively bright ($\text{avg}_c(\widetilde{B^c}) >> 0.5$) then $\widetilde{d_D}$ alone represents depth well. In this case, $\theta_a \approx 0$ and $\theta_b \approx 1$, and $\widetilde{d_n}(x) \approx \widetilde{d_D}(x)$.

Lastly if there is very little red light in the scene, so $\text{avg}(I^r) << 0.1$, then both Eq. (19) and Eq. (21) which directly use red channel values are likely to fail to estimate scene depth properly. In this case, $\theta_b \approx 0$, and $\widetilde{d_n}(x) \approx \widetilde{d_B}(x)$ mean that the depth estimation reverts to using the blurriness map alone, as in [16]. In between these various extremes, the depth map comes from a weighted combination of the three approaches.
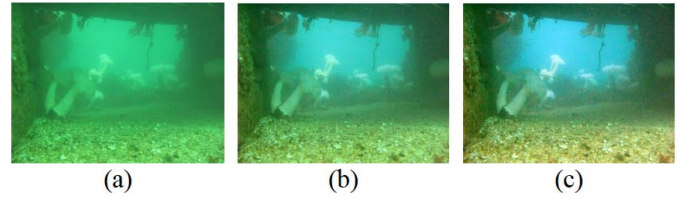
Fig. 10.   An example of TM estimation with and without $\widetilde{d_0}$. (a) Original image, and its restored images obtained using the proposed method, where the TM estimation (b) does not consider $\widetilde{d_0}$ and (c) considers $\widetilde{d_0} = 0.68$.

D. TM Estimation and Scene Radiance Recovery

As described in Section II-A, the TM estimation of the DCP-based methods is based on Eq. (7). By contrast, we calculate the TM according to Eq. (2), which uses the depth from the camera to scene points. To measure the distance from the camera to each scene point, the distance d_0 between the closest scene point and the camera must be estimated as well. Via the maximum difference between the estimated $\widetilde{B^c}$ and the observed intensities I^c in the input image, the estimated $\widetilde{d_0} \in [0, 1]$ can be calculated by:

$$\widetilde{d_0} = 1 - \max_{x, c\in\{r,g,b\}} \frac{|\,\widetilde{B^c} - I^c(x)\,|}{\max(\widetilde{B^k}, 1 - \widetilde{B^k})}, \quad (24)$$

where $k = \arg\max_{c\in\{r,g,b\}}\left(\max_x |\,\widetilde{B^c} - I^c(x)\,|\right)$. If the BL accounts for a large portion of the observed intensities for the closest scene point, the maximum difference would be small, and $\widetilde{d_0}$ would be large, i.e., the distance from the camera to the closest object in the scene is long.

Combining Eq. (23) and (24), the final scene depth $\widetilde{d_f}$ is given by:

$$\widetilde{d_f}(x) = D_\infty \times \left(\widetilde{d_n}(x) + \widetilde{d_0}\right), \quad (25)$$

where D_∞ is a scaling constant for transforming the relative distance to the actual distance.

With $\widetilde{d_f}$, we can calculate the TM for the red channel as:

$$\widetilde{t^r}(x) = e^{-\beta^r \widetilde{d_f}(x)}, \quad (26)$$

where $\beta^r \in [\frac{1}{8}, \frac{1}{5}]$ for Ocean Type–I water [2], [11], [30]. Roughly 98% of the world's open ocean and coastal waters fall into this category [28]. Then, we can compute the TMs, $\widetilde{t^g}$ and $\widetilde{t^b}$, for the green and blue channels by Eq. (10) and Eq. (11). Note that the typical ranges of the wavelength of red, green and blue light are $\lambda^r = 620 \sim 750\ nm$, $\lambda^g = 490 \sim 550\ nm$, and $\lambda^b = 400 \sim 490\ nm$. In this paper, we choose three standard
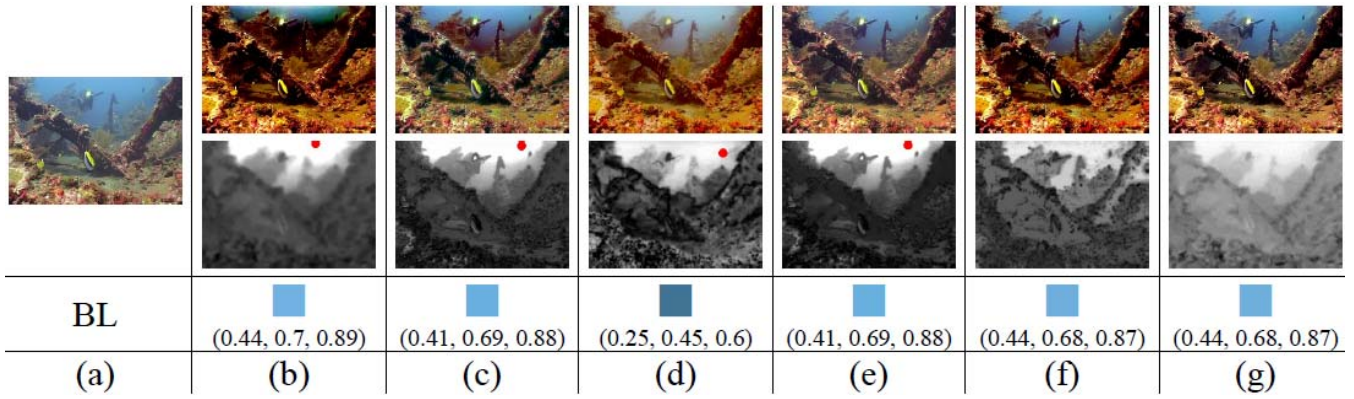
Fig. 11.   Restoration example where all methods are successful. (a) The original image. The enhanced results, and the corresponding depth map and BL (marked with a red dot for (b)–(e)) obtained using: (b) [9], (c) [12], (d) [14], (e) [15], (f) [16], and (g) the proposed method.
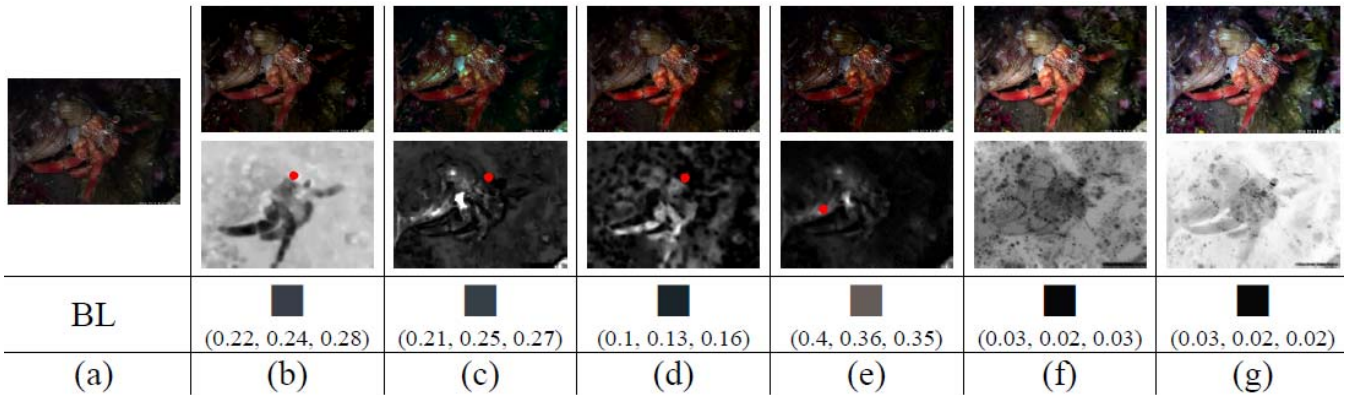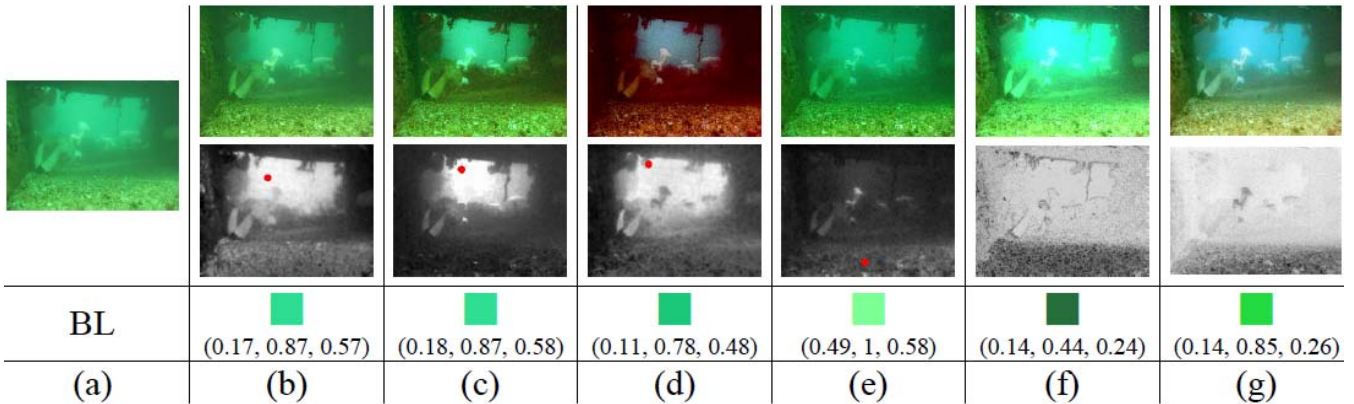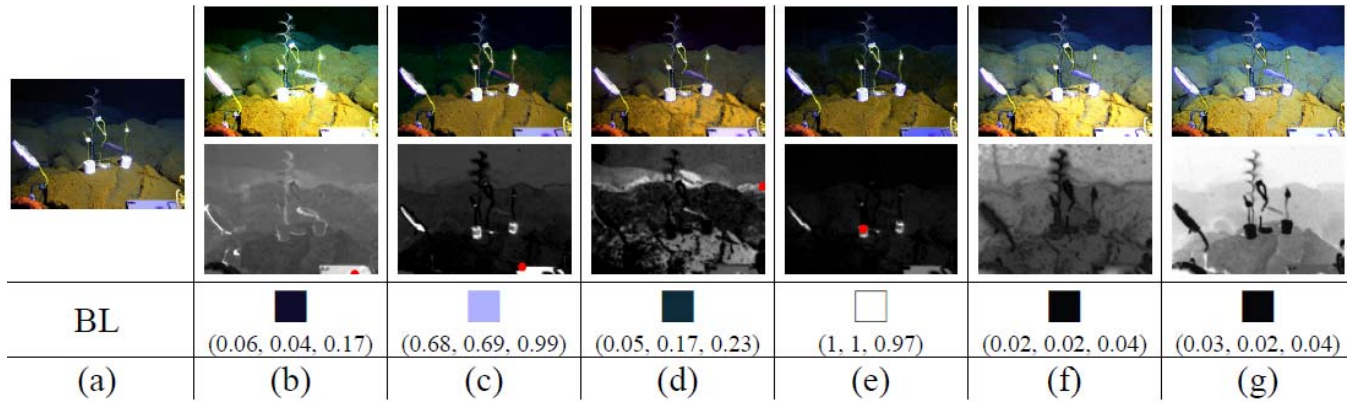

Fig. 12.   Example of restoring an underwater image with dim BL. (a) The original image. The restored results, and the corresponding depth map and BL (marked with a red dot for (b)–(e)) obtained using: (b) [9], (c) [12], (d) [14], (e) [15], (f) [16], and (g) the proposed method.

Fig. 13.   Example of restoring a greenish underwater image. (a) The original image. The restored results, and the corresponding depth map and BL (marked with a red dot for (b)–(e)) obtained using: (b) [9], (c) [12], (d) [14], (e) [15], (f) [16], and (g) the proposed method.

wavelengths for red, green and blue light $\lambda^r = 620 \ nm$, $\lambda^g = 540 \ nm$, and $\lambda^b = 450 \ nm$, as used in [15]. We found that the restoration results are not sensitive to values of $\beta^r \in [\frac{1}{8}, \frac{1}{6}]$, and we set $\beta^r = \frac{1}{7}$ throughout this paper. We also set $D_\infty = 8 \ m$ for our proposed method, so the range of $\tilde{t}^r$ is [0.1, 1]. Fig. 8(f) gives an example of TMs for the red, green and blue channels of a greenish underwater image based on Eq. (11) and Eq. (26). We can see that with properly estimated BL and our parameters, the proposed method can well restore the image as Fig. 8(e).

At the end, we recover the scene radiance using Eq. (8). Fig. 10 gives an example to show the effectiveness of using TM estimation considering $\tilde{d}_0$ in the proposed method. The proposed method with $\tilde{d}_0$ produces a more satisfactory restored result with better contrast and saturated color.

The proposed depth estimation based on light absorption can also handle artificial lighting gracefully by considering BL. If the BL of an underwater image with artificial lighting is dim, the restoration using the depth map derived by the red channel map R in Eq. (18) would regard those bright

Fig. 14.   Example of restoring an underwater image with artificial lighting. (a) The original image. The restored results, and the corresponding depth map and BL (marked with a red dot for (b)–(e)) obtained using: (b) [9], (c) [12], (d) [14], (e) [15], (f) [16], and (g) the proposed method. The original image comes from [36].
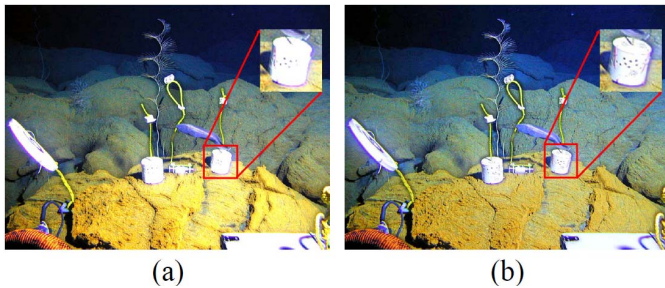

Fig. 15.   Close comparison between (a) [16] and (b) the proposed method for the original image shown in Fig. 14.

pixels as being close and not over-compensate their color. When BL is bright, the red light from the background pixels would attenuate more than that of the foreground pixels, which could be correctly interpreted as scene depth using Eq. (21). Sec. IV-A will demonstrate restoration examples with artificial lighting.

IV. EXPERIMENTAL RESULTS

Previous underwater image restoration methods used the IFM in Eq. (1) only based on the DCPs or the MIP. In this section, we compare our previous method based on image blurriness [16] and the proposed method based on both image blurriness and light absorption against the DCP- and the MIP-based methods. The performance of the proposed method is evaluated in three ways:

1) Subjective visual comparison including examination of the depth map and the BL,
2) Objective quantitative full-reference assessment of restored synthesized underwater images, and
3) Objective quantitative no-reference quality assessment of restored real-world underwater images.

A. Qualitative Assessment

In the visual comparison, we use six underwater images with different underwater color tones and lighting conditions for testing, where the depth maps shown all undergo a simple individual contrast stretching step for display.

In Fig. 11, we can see that the original image looks hazy and has bright BL. All methods work well for this case.

The blurriness-based method [16] and the proposed method generate similar depth maps and BL to those obtained by the DCP and MIP methods [9], [12], [14], [15]. All of the result images look restored and enhanced although some color differences exist.

In contrast, the original image in Fig. 12 is dimly lit, which invalidates the DCPs and MIP. Results from the MIP-based [9] and DCP-based methods [12], [14], [15] look insignificantly restored because of the incorrect depth map and wrong BL selection from the bright foreground pixels. The blurriness-based method [16] and the proposed method estimate the scene depth and BL more correctly.

Fig. 13 gives an example of restoring a greenish underwater image, which has some bright pixels in the foreground and dark pixels in the background, making the DCPs invalid. The depth map based on DCP_{rgb} [15] is opposite to the scene depth, resulting in a wrong BL selection and a poor restoration. For the method based on DCP_{gb} [12], even though the BL is properly selected, it presents an unsatisfactory restoration result because most of the pixels are mistakenly regarded as being close. The methods based on MIP [9] and $DCP_{r'gb}$ [14] both erroneously consider some foreground pixels as being far and background pixels as being close, also failing to restore the image. The blurriness-based method [16], which estimates depth more accurately in this case, gives an overexposed restoration result because of selecting dimmer BL. Additionally, like [9] and [12], it estimates only one single TM without considering different attenuation levels for RGB channels. Thus, their output images cannot be properly restored. The proposed method correctly estimates the depth and BL, and thus generates more accurate TMs for the red, green, and blue channels. Using these TMs (shown in Fig. 8(f)), the proposed method compensates more red and blue light for the original image than green light.

Fig. 14 shows an example of restoring an underwater image shot with artifical lighting. The method based on DCP_{rgb} [15] wrongly regards almost all of the pixels in the image as being close except for the white objects, leading to a restored image nearly identical to the original. The DCP_{gb} method [12] picks a bright foreground pixel as BL, which makes the background even darker. The $DCP_{r'gb}$ [14] method also produces a restored image with a dimmer background because
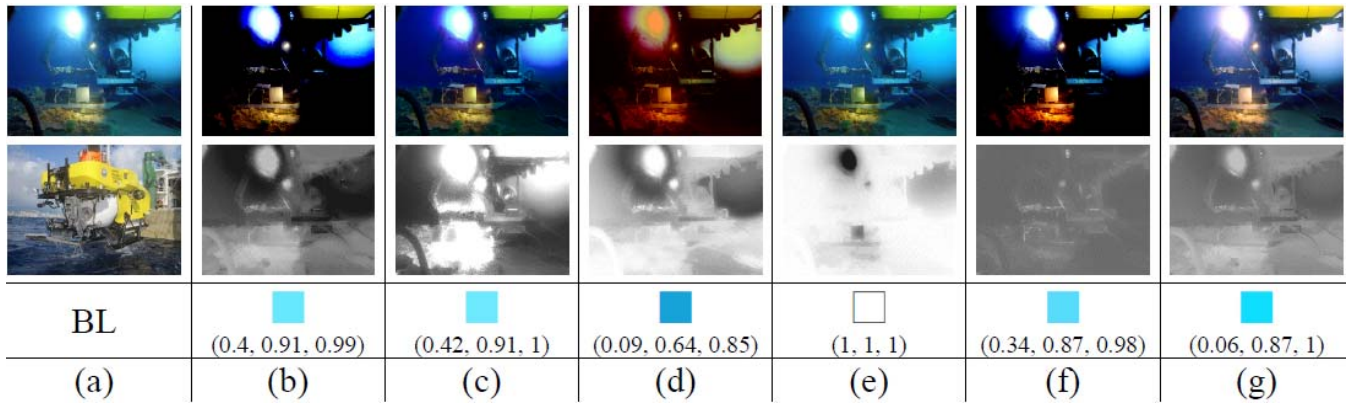
Fig. 16. Restoration example involving artificial lighting. (a) An underwater image of *Pisces V* and its out-of-water image. The restored results, and the corresponding **TM** (only $\tilde{t}^r$ is shown for [15] and the proposed method) and BL obtained using: (b) [9], (c) [12], (d) [14], (e) [15], (f) [16], and (g) the proposed method. The original image is from [36].
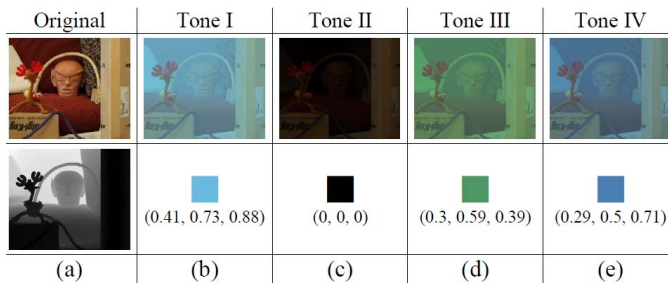
Fig. 17. Examples of synthesizing underwater images with four different underwater color tones using Eq. (27). (a) The ground truth image and its depth map. (b)–(e) Synthesized underwater images with $d_0 = 4$ and $r_s = 4$.
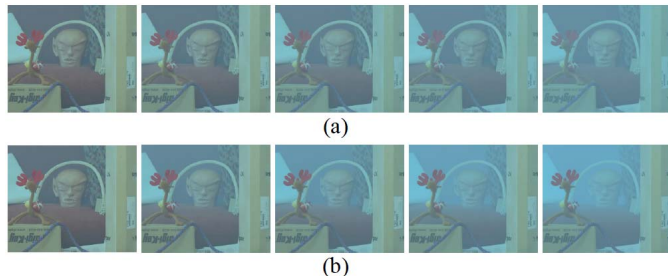
Fig. 18. All test synthesized underwater images with Tone I color. The images from left to right are synthesized (a) using $d_0 = 4, 5, \ldots, 8$ in "TestMode–InitD" and (b) using $r_s = 1, 2, \ldots, 5$ in "TestMode–ScaleD."

of the incorrect depth and BL estimation. Although the MIP-based [9] method selects dark BL to reveal the background scene in the processed image, it also produces an overexposed foreground. As shown in Fig. 15, the blurriness-based method [16] compensates the brightness for the background with dark BL but also overexposes some smooth regions in the foreground for which depth estimated based on blurriness is inaccurate. The proposed method estimates BL and depth more precisely and generates a well-enhanced restored image. We can see from the depth map that the bright pixels in the original image are regarded as being close, which prevents their overexposure.

Lastly, Fig. 16 demonstrates restoration of a special case with artificial lighting. Fig. 16(a) shows an image of *Pisces V* [38], a deep-submergence vehicle, with its external
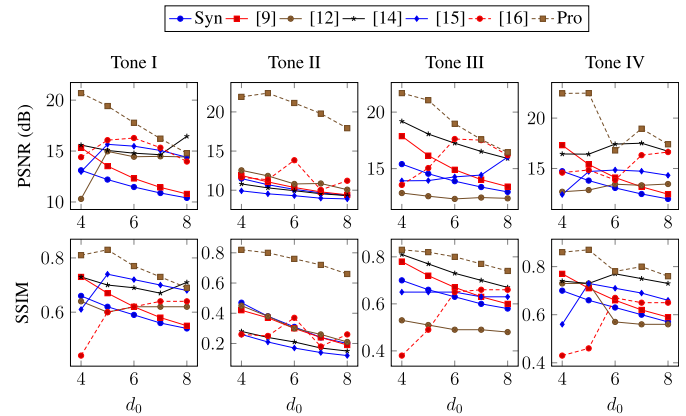
Fig. 19. PSNR results (top) and SSIM results (bottom) obtained using different restoration methods for "TestMode–InitD."
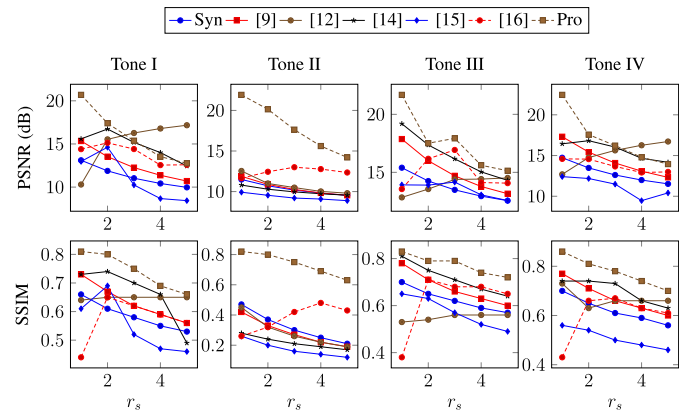
Fig. 20. PSNR results (top) and SSIM results (bottom) obtained using different methods for "TestMode–ScaleD."

light on in the underwater scene, as well as its out-of-water image for comparison. The red light in the underwater image is attenuated more than green and blue light. Unlike Fig. 11–Fig. 14 that present the depth maps, we show the corresponding TM estimated by each of the compared methods for the processed image to better explain the restoration results. Note that the TM aims to describe the portion of the scene radiance not scattered or absorbed but reaching the camera. A larger TM value means the corresponding scene point
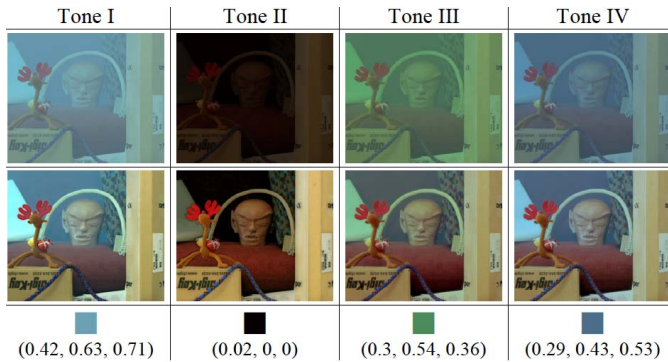
Fig. 21. Examples of restoring synthesized underwater images with Tone I–IV colors in "TestMode–ScaleD" ($r_s = 3$) obtained using the proposed method. The synthesized images are in the first row, and the corresponding restored images and BL estimates are shown in the second and third rows.
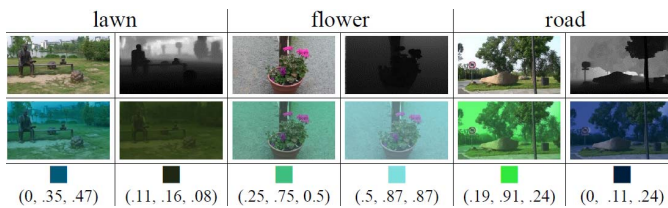
Fig. 22. Examples of synthesized underwater images generated using three different images with their depth maps and selected BLs.

Fig. 23. Examples of "BRISQUE score/UIQM value" pairs for synthesized (top) and real (bottom) underwater images. (The images are from [31], [35], and [36], and Google Images.)

Fig. 24. Test images for BRISQUE. (The images are from [1], [8], [9], [12], [14], [35], and [36], and Google Images.)

has more scene radiance that reaches the camera, while a smaller value means the BL accounts for more of the observed intensity of that scene point. Hence, the TM for the underwater image in Fig. 16(a) should have larger values for scene points closer to the artificial light and smaller values for the points farther from the light.

In Fig 16(c)–(f), the methods based on the DCP$_{gb}$ [12], DCP$_{r'gb}$ [14], DCP$_{rgb}$ [15], and image blurriness [16] fail to generate such TMs, and produce poor restoration results. The MIP-based method [9] estimates TM well, yet its estimated BL that has a larger value in the red channel is inaccurate, leading to a dimmer restoration result. The proposed method attains a more accurate TM and BL selection and presents a more precise color restoration result.

Method	Tone I		Tone II		Tone III		Tone IV	
	d_0	r_s	d_0	r_s	d_0	r_s	d_0	r_s
Pro+MIP	12.3/.62	12.0/.62	10.7/.36	10.9/.37	14.8/.67	14.5/.66	13.9/.66	13.5/.66
Pro+DCP$_{rgb}$	15.5/.76	15.2/.75	13.0/.63	10.4/.56	13.8/.70	13.2/.71	14.8/.75	13.5/.73
Pro+DCP$_{gb}$	16.8/.76	15.1/.70	13.1/.65	10.4/.58	16.4/.73	13.7/.70	17.1/.73	13.4/.69
Pro+DCP$_{r'gb}$	16.2/.77	15.5/.76	13.8/.65	12.6/.61	15.2/.73	14.9/.75	17.2/.79	15.1/.77
Pro+P$_{blr}$	14.2/.56	13.1/.57	13.0/.58	11.8/.60	13.8/.64	13.5/.66	15.3/.65	13.4/.65
Pro	**17.8/.77**	**16.0**/.74	**20.6**/.75	**17.9**/.74	**19.1**/.79	**17.6**/.78	**19.6**/.81	**17.0**/.78

B. Quantitative Assessment

1) Restoration of Synthesized Underwater Images: Although the simplified IFM in Eq. (1) is widely used to describe the formation of a hazy image and can also be invoked to explain the formation of an underwater image, light that travels through water causes image blur because of light scattering and refraction [3], which is ignored by this model. To synthesize a more realistic underwater image, image blur must be incorporated in the model. This image blur can be modeled by a point spread function, where the blur kernel width is proportional to the scene depth [3], [26], [27]. Combining the IFM and the point spread function, we describe an underwater IFM as:

$$I^c(x) = \left[J^c(x)t^c(x) + B^c\left(1 - t^c(x)\right) \right] * \Phi\left(\beta^c, d(x)\right), \quad (27)$$

where Φ is a point spread function of the form [26]:

$$\Phi(\beta, z) = (e^{-\gamma z} - e^{-\beta z})e^{-a\frac{\|\mathbf{x_z}\|^2}{z}}, \quad (28)$$

where $a > 0$ and $|\gamma| \leq \beta$ are empirical constants, and $\mathbf{x_z}$ is the coordinate for the point spread function.

In the quantitative analysis, we first synthesize underwater images for evaluation. Five ground truth images, for which the depth maps are known, were used to synthesize underwater images using Eq. (27). We focus initially on an indoor image "reindeer," which was used in [31] to synthesize a hazy image. The image and its depth map are shown in Fig 17(a). In this image, the foreground pixels are not bright, so it will not tend to invalidate the DCP and MIP assumptions. Thus, it is useful for testing the capability of the compared methods to restore underwater images with different BL. For a fair comparison, all of the compared methods use the 7×7 local patch $\Omega(x)$ in Eq. (5)–(7), (9), (12), (14) and (18), a lower bound $t_0 = 0.1$ for the TM in Eq. (8), and the guided filtering to smooth the TM. To compare the color restoration results, we adopt two metrics, PSNR and SSIM.

The ground truth image, denoted J_g, its ground truth depth map, $d_g \in [0.6, 3.1 \, m]$, and four BLs are used to simulate underwater images with four different underwater color tones, shown in Fig. 17. For each color tone, we modify the depth map in two test modes to adjust the relative amounts of BL and scene radiance in the synthesized observed intensity. The first test mode, "TestMode–InitD," adds an initial distance d_0 to the ground truth depth: $d_0 + d_g = d_s$, where d_s is the final depth map used in the synthesis, and d_0 takes values in the set $\{4, 5, 6, 7, 8 \, m\}$ for testing. The second test mode,

TABLE III

COMPARISON OF AVERAGE PSNR/SSIM OF THE RESTORATION RESULTS OVER ALL THE TESTED $d_0 \in [4, 8\ m]$ FOR "TESTMODE–INITD."

Method	Tone I			Tone II			Tone III			Tone IV		
	d_0	ExtBL†	ExtTM†	d_0	ExtBL	ExtTM	d_0	ExtBL	ExtTM	d_0	ExtBL	ExtTM
None	11.6/.59	–/–	–/–	10.3/.32	–/–	–/–	14.0/.63	–/–	–/–	13.2/.63	–/–	–/–
[9]	12.7/.63	13.0/.63	19.2/.60	10.5/.31	10.8/.37	16.6/.55	15.3/.68	15.3/.68	14.5/.43	14.5/.67	14.7/.67	15.7/.48
[12]	13.7/.62	19.9/.73	18.1/.64	11.2/.32	12.4/.65	14.5/.44	12.5/.50	19.3/.69	14.5/.43	13.2/.63	17.8/.72	16.4/.61
[14]	15.3/.70	10.6/.27	12.2/.71	10.0/.21	13.4/.56	10.6/.24	17.4/.74	13.9/.57	19.9/.70	16.9/.74	12.5/.47	18.6/.59
[15]	14.7/.69	18.1/.75	16.8/.53	9.3/.18	11.1/.29	8.7/.08	14.5/.64	16.9/.75	14.5/.40	14.2/.67	18.7/.77	13.8/.39
[16]	15.2/.59	15.2/.48	18.1/.79	11.6/.26	14.1/.66	12.4/.33	16.0/.57	17.8/.64	19.1/.64	15.2/.57	16.5/.54	18.1/.69
Pro	**17.8/.77**	**20.8/.80**	**19.3/.81**	**20.6/.75**	**22.7/.89**	**23.3/.77**	**19.1/.79**	**23.6/.85**	**24.7/.83**	**19.6/.81**	**22.2/.84**	**26.3/.87**

† ExtBL and ExtTM represent restoration with the exact BL and TM.

TABLE IV

COMPARISON OF AVERAGE PSNR/SSIM OF THE RESTORATION RESULTS OVER ALL THE TESTED $r_s \in [1, 5]$ FOR "TESTMODE–SCALED"

Method	Tone I			Tone II			Tone III			Tone IV		
	r_s	ExtBL†	ExtTM†	r_s	ExtBL	ExtTM	r_s	ExtBL	ExtTM	r_s	ExtBL	ExtTM
None	11.3/.59	–/–	–/–	10.3/.32	–/–	–/–	13.7/.63	–/–	–/–	12.9/.62	–/–	–/–
[9]	12.6/.63	12.9/.64	**21.4**/.71	10.5/.29	10.9/.38	13.1/.39	15.1/.68	15.1/.67	17.1/.56	14.4/.67	14.5/.67	18.4/.59
[12]	15.2/.65	**19.3**/.71	19.9/.74	10.8/.29	10.3/.57	12.6/.37	13.9/.55	17.0/.65	16.6/.54	15.2/.67	17.6/.70	19.0/.67
[14]	14.8/.66	10.6/.28	11.0/.70	10.1/.22	13.2/.53	10.5/.24	16.4/.72	13.8/.59	20.2/.68	15.6/.70	12.5/.47	20.5/.68
[15]	11.0/.55	17.1/.73	12.7/.49	9.3/.18	11.3/.30	8.8/.09	13.5/.57	16.1/.72	13.1/.35	11.2/.51	17.7/.75	11.7/.42
[16]	13.8/.57	14.4/.46	18.7/**.78**	12.4/.38	13.2/.63	18.4/.57	15.0/.62	16.8/.63	20.4/.78	13.7/.60	15.8/.54	19.0/.77
Pro	**16.0/.74**	18.7/**.77**	18.3/**.78**	**17.9/.74**	**18.5/.81**	**24.8/.79**	**17.6/.78**	**20.9/.81**	**22.2/.82**	**17.0/.78**	**20.2/.80**	**21.7/.82**

† ExtBL and ExtTM represent restoration with the exact BL and TM.

TABLE V

COMPARISON OF AVERAGE PSNR/SSIM OF THE RESTORATION RESULTS OVER ALL THE TESTED d_0 FOR "TESTMODE–INITD"

Method	lawn ■			lawn ■			flower ■			flower ■			road ■			road ■		
	d_0	ExtBL	ExtTM	d_0	ExtBL	ExtTM	d_0	ExtBL	ExtTM	d_0	ExtBL	ExtTM	d_0	ExtBL	ExtTM	d_0	ExtBL	ExtTM
None	19.4/.66	–/–	–/–	13.2/.48	–/–	–/–	19.1/.71	–/–	–/–	16.9/.66	–/–	–/–	16.7/.66	–/–	–/–	15.3/.55	–/–	–/–
[9]	18.8/.68	22.0/.71	18.5/.74	13.1/.47	13.4/.49	10.1/.25	21.0/.79	23.2/.81	18.9/.79	19.1/.73	19.8/.73	**29.6/.93**	19.0/.70	19.9/.73	16.1/.57	15.0/.55	16.8/.60	13.8/.48
[12]	12.6/.49	15.6/.72	17.7/.70	10.7/.30	11.4/.65	10.1/.24	15.6/.72	15.9/.75	23.4/.89	14.1/.71	14.1/.69	26.0/.92	13.9/.55	17.7/.72	14.0/.45	11.7/.36	12.0/.68	10.9/.24
[14]	11.6/.37	15.9/.59	23.0/.85	11.6/.40	16.0/.64	12.3/.42	10.0/.49	10.7/.49	24.1/.90	17.3/.70	7.0/.19	10.3/.62	10.6/.22	15.4/.52	14.3/.46	10.7/.24	19.1/.78	12.6/.39
[15]	17.7/.64	18.7/.70	11.9/.40	9.8/.24	11.1/.56	9.0/.15	11.1/.67	20.6/.86	10.4/.54	15.8/.79	19.9/**.91**	23.2/.84	15.8/.55	20.6/.77	11.5/.29	13.7/.48	14.3/.59	10.4/.19
[16]	10.7/.30	16.1/.67	17.8/.72	13.5/.52	17.8/.71	13.7/.55	12.0/.58	13.1/.64	14.4/.72	16.6/.74	13.0/.60	22.3/.91	12.6/.37	17.4/.65	14.1/.45	11.5/.27	18.0/.78	12.6/.38
Pro	**22.7/.79**	**26.5/.85**	**24.1/.87**	**19.0/.79**	**20.8/.83**	**23.2/.88**	**24.0/.89**	**27.8/.89**	**26.0/.91**	**19.3/.87**	**24.9/.89**	21.3/.92	**22.5/.84**	**22.4/.84**	**26.4/.91**	**19.8/.78**	**23.1/.85**	**21.5/.84**

† ExtBL and ExtTM represent restoration with the exact BL and TM.

TABLE VI

COMPARISON OF AVERAGE PSNR/SSIM OF THE RESTORATION RESULTS OVER ALL THE TESTED r_s FOR "TESTMODE–SCALED"

Method	lawn ■			lawn ■			flower ■			flower ■			road ■			road ■		
	r_s	ExtBL	ExtTM	r_s	ExtBL	ExtTM	r_s	ExtBL	ExtTM	r_s	ExtBL	ExtTM	r_s	ExtBL	ExtTM	r_s	ExtBL	ExtTM
None	17.5/.62	–/–	–/–	13.0/.45	–/–	–/–	16.9/.62	–/–	–/–	16.0/.58	–/–	–/–	14.8/.60	–/–	–/–	14.6/.49	–/–	–/–
[9]	17.9/.64	20.1/.66	15.9/.63	12.9/.45	13.1/.46	10.9/.32	18.7/.70	21.5/.71	17.8/.76	18.2/.64	18.6/.64	**28.2/.85**	17.3/.65	18.5/.66	17.4/.63	14.3/.49	15.8/.53	12.7/.40
[12]	12.3/.45	14.9/.66	15.6/.62	10.8/.31	10.7/.54	10.3/.27	15.3/.70	14.9/.71	22.5/.83	14.5/.68	14.2/.66	25.2/**.85**	15.4/.58	16.8/.64	17.0/.61	11.6/.34	12.2/.58	11.0/.25
[14]	11.8/.37	15.3/.55	20.4/.78	10.8/.33	15.0/.58	11.3/.35	9.3/.41	10.0/.42	23.3/**.84**	11.1/.41	7.0/.17	9.7/.53	11.7/.35	14.6/.46	14.6/.54	13.0/.37	17.5/.67	13.4/.46
[15]	16.7/.60	17.6/.66	10.9/.32	9.5/.21	10.7/.47	8.9/.14	11.0/.59	21.7/**.80**	8.8/.40	14.7/.69	21.3/**.83**	18.7/.71	13.5/.48	18.2/.69	11.4/.28	13.1/.43	13.6/.50	10.1/.18
[16]	13.4/.46	16.3/.65	18.9/.75	14.9/.56	15.9/.61	17.9/.69	16.0/.66	14.9/.65	22.1/.81	18.0/.69	15.5/.62	24.3/**.85**	14.2/.45	16.3/.57	16.5/.59	12.8/.38	16.0/.67	13.7/.49
Pro	**21.1/.74**	**23.2/.79**	**24.2/.81**	**17.4/.71**	**17.9/.72**	**21.2/.77**	**21.2/.77**	**23.4/.77**	**23.5/.84**	**19.3/.75**	**21.8/.76**	22.1/.84	**18.6/.70**	**19.2/.72**	**20.8/.73**	**17.8/.67**	**19.2/.70**	**18.8/.74**

† ExtBL and ExtTM represent restoration with the exact BL and TM.

"TestMode–ScaleD," increases the scene depth by multiplying by a scaling factor: $d_s = d_f + d_g \times r_s$, where $d_f = 4$ is a fixed initial distance, and $r_s \in \{1, 2, 3, 4, 5\}$.

The TM for the red channel is calculated by $t^r(x) = e^{-\beta_s^r d_s(x)}$ as Eq. (2) with $\beta_s^r = \frac{1}{5}$, and the TMs for the green and blue channels are estimated by Eq. (10) and Eq. (11) based on the chosen BL. For the point spread function in Eq. (28), we set $\gamma = \frac{\beta}{2}$, and $a = 8$. By putting J_g, t^c and B^c into Eq. (27), we can synthesize underwater images. Examples are shown in Fig. 18.

For each test mode, we compute the PSNR and SSIM results between the ground truth image J_g and the synthesized underwater images restored using the five IFM-based restoration methods [9], [12], [14]–[16], and the proposed

TABLE VII

COMPARISON OF AVERAGE PSNR/SSIM OF THE RESTORATION RESULTS OVER ALL THE TESTED d_0 AND r_s OBTAINED USING THE PROPOSED METHOD AND ITS MIXED METHODS USING THE TM ESTIMATION FOR THE RED CHANNEL $\tilde{t}^r$ BASED ON DCPs, MIP, OR IMAGE BLURRINESS

Method	lawn ■		lawn ■		flower ■		flower ■		road ■		road ■	
	d_0	r_s	d_0	r_s	d_0	r_s	d_0	r_s	d_0	r_s	d_0	r_s
Pro+MIP	19.8/.68	18.6/.64	13.3/.49	13.1/.46	20.9/.78	19.5/.68	17.9/.72	17.1/.63	18.5/.71	16.8/.64	15.9/.58	15.2/.52
Pro+DCP$_{rgb}$	21.3/.76	18.9/.70	12.0/.66	10.9/.55	20.0/.86	20.4/.81	17.4/.80	19.3/**.80**	20.4/.77	17.9/.67	15.9/.71	14.1/.58
Pro+DCP$_{gb}$	14.7/.64	14.2/.62	12.0/.66	10.9/.55	19.1/.79	18.1/.77	15.5/.72	15.0/.70	19.8/.78	17.6/.68	13.9/.70	12.3/.55
Pro+DCP$_{r'gb}$	21.9/.77	20.9/.73	15.0/.77	13.5/.67	22.1/**.91**	21.1/**.83**	17.4/.80	19.3/**.80**	20.7/.77	18.1/.68	19.6/**.78**	16.9/**.68**
Pro+P$_{blr}$	21.7/.77	20.8/.72	16.7/.71	15.7/.62	17.8/.77	18.1/.74	15.6/.68	16.4/.67	20.0/.81	17.0/.64	18.3/.75	15.5/.64
Pro	**22.7/.79**	**21.1/.74**	**19.0/.79**	**17.4/.71**	**24.0**/.89	**21.1**/.77	**19.3/.87**	**19.3**/.75	**22.5/.84**	**18.6/.70**	**19.8/.78**	**17.8**/.67

TABLE VIII

AVERAGE BRISQUE SCORES AND UIQM VALUES OF THE ORIGINAL IMAGES IN FIG. 24 AND THEIR RESTORED VERSIONS FROM ALL THE COMPARED METHODS

	Original	[9]	[12]	[14]	[15]	[16]	Proposed
BRISQUE	36.31	34.49	31.45	33.57	31.61	31.73	**30.24**
UIQM	2.60	2.83	3.05	2.65	2.75	3.17	**3.23**

method, shown in Fig. 19 and Fig. 20. In Fig. 19, we see that the proposed method performs better for all the four underwater color tones. As the scene depth increases, the PSNR and SSIM results of the compared methods become close. In Fig. 20, the proposed method is better than the other ones except for [12] in the PSNR results for Tone I and IV colors. This is because we set $D_\infty = 8\ m$ in Eq. (25) to restore the color of underwater objects in the range of scene depth $[0, 16\ m]$, and thus the proposed method does not restore well scene points farther than this range. However, the proposed method still outperforms all the other methods in the SSIM results in "TestMode–ScaleD." Note that the proposed method excels more in restoring images with Tone II color, which represents very dim BL. This is because dim BL violates the assumptions underlying the DCPs and MIP. Examples of restoring synthesized underwater images with Tone I–IV colors obtained using the proposed method are in Fig. 21.

To measure the effectiveness of the TM estimation based on our proposed depth estimation, we compare the restoration results obtained using the TMs estimated based on the DCPs and MIP, as well as ours. That is, we adopt different TM estimation methods to generate the TM for the red channel $\tilde{t}^r$. The TMs for the green and blue channels are then estimated by Eq. (10) and Eq. (11) based on the proposed BL. We compare the restoration results obtained using these different TM estimation methods. Table II lists average PSNR/SSIM results over all the tested d_0 and r_s obtained using the proposed method and its mixed methods using other TM estimation methods based on DCPs, MIP, or image blurriness. Namely, the column marked d_0 contains average PSNR/SSIM of the restoration results over all the test d_0 in "TestMode–InitD," while the column marked r_s contains the results over all the test r_s in "TestMode–ScaleD." We can see that the proposed TM estimation outperforms the others.

Moreover, we demonstrate the average PSNR and SSIM results for all the compared methods in Table III and Table IV for "TestMode-InitD" and "TestMode-ScaleD." We also show the results attained using the exact BL and TM in the compared methods in order to further analyze the preciseness of the BL and TM estimation methods, individually. In Table III, we see the superiority of the proposed method

in each compared category. In Table IV, the proposed method is better in all the tested underwater color tones on average except for Tone I color, which represents bright blue BL, where it incurs small PSNR deficits compared to [9] in the category of the exact TM and [12] in that of the exact BL.

In addition to "reindeer", three more images with ground truth depth maps were selected from [31] to synthesize underwater images with six different BLs (two for each image), as shown in Fig. 22. The ground truth depth d_g for the three images, "lawn," "flower," and "road," are in the range $[0.4, 11.3\ m]$, $[0.5, 13.2\ m]$, $[0.3, 9.5\ m]$, respectively. To vary the initial distance d_0 for each image, we set $d_0 \in \{1, 2, \ldots 5\ m\}$ for "flower," $d_0 \in \{2, 3 \ldots 6\ m\}$ for "road," and $d_0 \in \{3, 4, \ldots 7\ m\}$ for "lawn," while r_s still takes values in the set $\{1, 2, \ldots, 5\}$. As can be seen in Tables V to VII, the results are generally in line with those based on "reindeer," supporting the superiority of the proposed method. Note that Table VII is like Table II, where the column marked d_0 contains average PSNR/SSIM results over all the test d_0 in "TestMode–InitD," while the column marked r_s contains the results over all the test r_s in "TestMode–ScaleD," where d_f is the smallest value in their corresponding d_0 set for each test image.

2) No-Reference Quality Assessment: One can also objectively evaluate underwater image restoration methods on real images [18]–[20]. Here, we adopt two non-reference image quality metrics. One is the Blind/Referenceless Image Spatial QUality Evaluator (BRISQUE) [18], a natural scene statistics-based distortion-generic blind/no-reference image quality assessment tool for evaluating possible losses of naturalness of an image because of the presence of distortions. The score ranges from 0 to 100, where 0 represents the best quality and 100 the worst. We download its software release from [32] for testing. The other is the Underwater Image Quality Measure (UIQM) [19], a linear combination of three underwater image attribute measures: the colorfulness (UICM), sharpness (UISM), and contrast (UIConM) measures, where UIQM $= c_1 \times$UICM$+c_2 \times$UISM$+c_3 \times$UIConM. A greater value of the UIQM represents higher image quality. In the experiment, our implementation of UIQM uses $\alpha_L = \alpha_R = 0.1$ in UICM, a 8×8 window size for the EME measure and a constant 40 for Sobel edge detection in UISM, $\mu(M) = \gamma(M) = k(M) = 1026$ for the PLIP operations in UIConM, and the default coefficients $c_1 = 0.0282$, $c_2 = 0.2952$, and $c_3 = 3.5753$.

To give an idea of output values for both metrics, Fig. 23 lists BRISQUE scores and UIQM values for real underwater images as well as for synthesized underwater images with
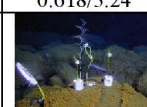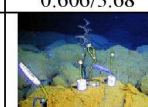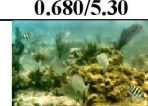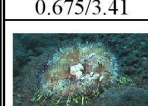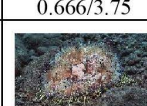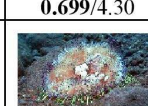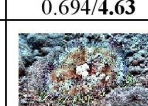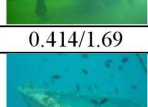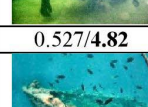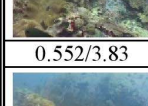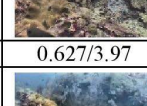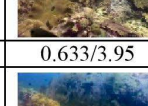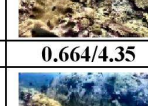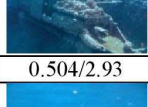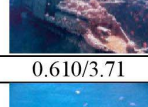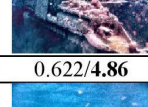
0.424/2.53	**0.588**/4.35	0.523/4.00	0.557/**5.05**	0.503/0.97	0.643/2.02	0.609/1.85	**0.667/3.22**
0.543/4.15	0.705/4.80	0.660/4.78	**0.709/4.88**	0.464/1.52	0.618/3.24	0.606/3.68	**0.636/4.38**
0.565/3.86	0.670/4.72	0.620/4.42	**0.680/5.30**	0.675/3.41	0.666/3.75	**0.699**/4.30	0.694/**4.63**
0.426/3.32	**0.652**/4.80	0.573/4.45	0.642/**5.05**	0.553/4.32	0.602/4.50	**0.618/4.67**	0.615/4.53
0.496/4.23	**0.643**/4.62	0.572/4.66	0.642/**4.85**	0.589/3.78	0.639/4.09	**0.717**/3.85	0.700/**4.27**
0.414/1.69	**0.590**/4.81	0.488/2.72	0.527/**4.82**	0.584/3.67	0.637/3.90	0.684/3.87	**0.689/4.26**
0.408/2.21	**0.617**/3.61	0.521/3.08	0.592/**4.15**	0.599/2.29	0.617/2.69	**0.685**/2.35	0.676/**3.14**
0.608/4.04	0.655/4.31	0.669/4.37	**0.674/4.91**	0.552/3.83	0.627/3.97	0.633/3.95	**0.664/4.35**
0.504/2.93	**0.632**/4.36	0.610/3.71	0.622/**4.86**	0.491/2.31	0.636/4.21	0.654/3.22	**0.674/4.45**
0.697/3.75	0.718/4.40	**0.744**/4.51	**0.744/5.11**	0.554/2.42	0.637/3.47	0.649/3.08	**0.657/4.18**
(a)	(b)	(c)	(d)	(e)	(f)	(g)	(h)

Fig. 25. Comparisons between the processed images obtained using [1] and the proposed method with and without contrast enhancement. The UCIQE score/UIQM value pair is shown below each image. (a) and (e) Original images. The processed results are obtained using (b) and (f) [1], (c) and (g) the proposed method, and (d) and (h) the proposed method+histogram equalization (The original images in column (a) are from Emberton's data set [17] and the ones in column (e) are from [35]–[37].)
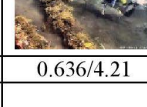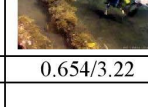
different attenuation levels (for which BRISQUE scores increase and UIQM values decrease monotonically with attenuation level). In Fig. 24, we show 70 real underwater test images with different contents and a variety of color tones. Table VIII lists the average BRISQUE scores and UIQM values for the original underwater images in Fig. 24 and their restored images from all the compared methods.

We can see that the proposed method outperforms the other methods.

V. COMBINING IFM-BASED RESTORATION AND HISTOGRAM EQUALIZATION

Methods based on the IFM, such as ours, have the goal of restoration, rather than enhancement. This paper first aimed

to demonstrate that our IFM-based method outperforms other IFM-based methods both for synthesized images (for which a ground truth is available, and full-reference fidelity metrics such as PSNR can be used), and for real underwater images (for which no-reference image quality metrics can be used).

It is also of interest to compare our IFM-based method against an underwater image enhancement method. The fusion-based enhancement method for underwater images proposed by Ancuti *et al.* [1] first generates two images based on the input image: one has colors adjusted by white balancing and the other is contrast-enhanced via local adaptive histogram equalization. Then these two images are fused based on their contrast, saliency, and exposedness to produce the final enhanced result with better contrast and white balance.

Histogram equalization [33] is a simple contrast enhancement method that can be added as a post-processing to an IFM-based method if some application needs the contrast of an underwater image to be enhanced. In Fig. 25, we compare our proposed method (both with and without histogram equalization contrast enhancement [34]) with the method by Ancuti *et al.* [1], using both subjective and objective comparisons. For objective assessment, we choose two no-reference quality assessment tools, the UIQM [19] and Underwater Color Image Quality Evaluation Metric (UCIQE) [20]. UCIQE quantifies image quality via a linear combination of the variation of chrominance, average saturation, and luminance contrast.

Fig. 25(a) shows the 10 original images from Emberton's data set [17]. In Fig. 25(b)-(d), we see that the enhanced images via Ancuti's method [1] (column (b)) have better contrast compared to those by the proposed method (column (c)). Since UCIQE and UIQM reward high contrast, the images obtained using [1] also have higher scores than those using the proposed method. Using histogram equalization [34] on our method, the contrast and UCIQE/UIQM values go up.

Fig. 25(e) shows an additional 10 original images. In the top four rows of Fig. 25 (e)-(h), the images are very dark or have artificial lighting. The method [1] does poorly because contrast enhancement is often not effective for such images, and the white balancing of [1] sometimes introduces unwanted colors to the output images, such as the original images in the first row of Fig. 25 (a) and (e), which makes the processed images unnatural even though it boosts its UCIQE/UIQM scores. For the bottom six rows of Fig. 25 (e)-(h), since the color of the original images is more balanced, the white balancing has little effect on these images. In comparison, the restored and enhanced results via the proposed method with and without histogram equalization look better for such images.

Comparing image enhancement methods using UCIQE and UIQM or other no-reference metrics is difficult because the metrics weight contrast and colorfulness differently. For example the UIQM algorithm removes the 10% of pixels with brightest and darkest values before computing the image colorfulness, whereas the UCIQE algorithm uses all pixels. Depending on factors like this and the weight given to different components, a white balancing step or a histogram equalization step can have a significant effect on the quantitative output of the metrics.

VI. CONCLUSION

For underwater image restoration, we have proposed to exploit image blurriness and light absorption to estimate the background light, scene depth, and transmission maps instead of using the DCPs or MIP. Using both synthesized and real underwater images with different color tones and contents, we demonstrated satisfying restored and enhanced underwater images. The proposed depth estimation works well for a wide variety of underwater images. Both the subjective and objective experimental results showed that the proposed method can produce better restoration and enhancement results in different underwater color tones and lighting conditions compared to other IFM-based underwater image restoration methods.

ACKNOWLEDGMENT

REFERENCES

[1] C. Ancuti, C. O. Ancuti, T. Haber, and P. Bekaert, "Enhancing underwater images and videos by fusion," in *Proc. IEEE Conf. Comput. Vis. Pattern Recognit.*, Providence, RI, USA, Jun. 2012, pp. 81–88.

[2] S. Q. Duntley, "Light in the sea," *J. Opt. Soc. Amer.*, vol. 53, no. 2, pp. 214–233, 1963.

[3] Y. Y. Schechner and N. Karpel, "Recovery of underwater visibility and structure by polarization analysis," *IEEE J. Ocean Eng.*, vol. 30, no. 3, pp. 570–587, Jul. 2005.

[4] S. G. Narasimhan and S. K. Nayar, "Chromatic framework for vision in bad weather," in *Proc. IEEE Conf. Comput. Vis. Pattern Recognit. (CVPR)*, vol. 1. Jun. 2000, pp. 598–605.

[5] S. G. Narasimhan and S. K. Nayar, "Vision and the atmosphere," *Int. J. Comput. Vis.*, vol. 48, no. 3, pp. 233–254, 2002.

[6] R. Fattal, "Single image dehazing," *ACM Trans. Graph.*, vol. 27, no. 3, pp. 721–729, 2008.

[7] K. He, J. Sun, and X. Tang, "Single image haze removal using dark channel prior," *IEEE Trans. Pattern Anal. Mach. Intell.*, vol. 33, no. 12, pp. 2341–2353, Dec. 2011.

[8] L. Chao and M. Wang, "Removal of water scattering," in *Proc. IEEE Int. Conf. Comput. Eng. Technol. (ICCET)*, vol. 2. Apr. 2010, pp. 35–39.

[9] N. Carlevaris-Bianco, A. Mohan, and R. M. Eustice, "Initial results in underwater single image dehazing," in *Proc. IEEE Oceans*, Sep. 2010, pp. 1–8.

[10] H.-Y. Yang, P.-Y. Chen, C.-C. Huang, Y.-Z. Zhuang, and Y.-H. Shiau, "Low complexity underwater image enhancement based on dark channel prior," in *Proc. Int. Conf. Innov. Bio-Inspired Comput. Appl. (IBICA)*, Dec. 2011, pp. 17–20.

[11] J. Y. Chiang and Y.-C. Chen, "Underwater image enhancement by wavelength compensation and dehazing," *IEEE Trans. Image Process.*, vol. 21, no. 4, pp. 1756–1769, Apr. 2012.

[12] H. Wen, Y. Tian, T. Huang, and W. Gao, "Single underwater image enhancement with a new optical model," in *Proc. IEEE Int. Symp. Circuits Syst. (ISCAS)*, May 2013, pp. 753–756.

[13] P. Drews, E. do Nascimento, F. Moraes, S. Botelho, and M. Campos, "Transmission estimation in underwater single images," in *Proc. IEEE Int. Conf. Comput. Vis. Workshops*, Sydney, NSW, Australia, Dec. 2013, pp. 825–830.

[14] A. Galdran, D. Pardo, A. Picón, and A. Alvarez-Gila, "Automatic red-channel underwater image restoration," *J. Vis. Commun. Imag. Represent.*, vol. 26, pp. 132–145, Jan. 2015.

[15] X. Zhao, J. Tao, and Q. Song, "Deriving inherent optical properties from background color and underwater image enhancement," *Ocean Eng.*, vol. 94, pp. 163–172, Jan. 2015.

[16] Y.-T. Peng, X. Zhao, and P. C. Cosman, "Single underwater image enhancement using depth estimation based on blurriness," in *Proc. IEEE Int. Conf. Imag. Process. (ICIP)*, Sep. 2015, pp. 4952–4956.

[17] S. Emberton, L. Chittka, and A. Cavallaro, "Hierarchical rank-based veiling light estimation for underwater dehazing," in *Proc. Brit. Mach. Vis. Conf. (BMVC)*, 2015, pp. 125.1–125.12.

[18] A. Mittal, A. K. Moorthy, and A. C. Bovik, "No-reference image quality assessment in the spatial domain," *IEEE Trans. Image Process.*, vol. 21, no. 12, pp. 4695–4708, Dec. 2012.

[19] K. Panetta, C. Gao, and S. Agaian, "Human-visual-system-inspired underwater image quality measures," *IEEE J. Ocean Eng.*, vol. 41, no. 3, pp. 1–11, Jul. 2015.

[20] M. Yang and A. Sowmya, "An underwater color image quality evaluation metric," *IEEE Trans. Image Process.*, vol. 24, no. 12, pp. 6062–6071, Dec. 2015.

[21] Z. Wang, A. C. Bovik, H. R. Sheikh, and E. P. Simoncelli, "Image quality assessment: From error visibility to structural similarity," *IEEE Trans. Image Process.*, vol. 13, no. 4, pp. 600–612, Apr. 2004.

[22] P. Bouguer, *Essai d'Optique, Sur la Gradation de la Lumiere*. Paris, France: Claude Jombert, 1729.

[23] P. Soille, "Morphological image analysis," in *Principles and Applications*. Berlin, Germany: Springer-Verlag, 1999, pp. 173–174.

[24] A. Levin, D. Lischinski, and Y. Weiss, "A closed-form solution to natural image matting," *IEEE Trans. Pattern Anal. Mach. Intell.*, vol. 30, no. 2, pp. 228–242, Feb. 2008.

[25] K. He, J. Sun, and X. Tang, "Guided image filtering," *IEEE Trans. Pattern Anal. Mach. Intell.*, vol. 35, no. 6, pp. 1397–1409, Oct. 2012.

[26] B. L. McGlamery, "A computer model for underwater camera system," in *Proc. SPIE Ocean Opt. VI*, vol. 0208, pp. 221–231, Mar. 1980.

[27] K. J. Voss, "Simple empirical model of the oceanic point spread function," *Appl. Opt.*, vol. 30, no. 18, pp. 2647–2651, 1991.

[28] C. D. Mobley, "Radiative Transfer in the Ocean," in *Encyclopedia of Ocean Sciences*, 2001, pp. 2321–2330.

[29] W. S. Jagger and W. R. A. Muntz, "Aquatic vision and the modulation transfer properties of unlighted and diffusely lighted natural waters," *Vis. Res.*, vol. 33, no. 13, pp. 1755–1763, 1993.

[30] N. G. Jerlov, *Optical Oceanography*. Amsterdam, The Netherlands: Elsevier, 1968.

[31] R. Fattal, "Dehazing using color-lines," *ACM Trans. Graph.*, vol. 28, no. 4, 2014, Art. no. 13.

[32] [Online]. Available: http://live.ece.utexas.edu/research/quality/BRISQUE_release.zip

[33] R. Hummel, "Image enhancement by histogram transformation," *Comput. Graph. Image Process.*, vol. 6, no. 2, pp. 184–195, 1977.

[34] K. Zuiderveld, "Contrast limited adaptive histogram equalization," in *Graphics Gems IV*. San Diego, CA, USA: Academic, 1994, pp. 474–485.

[35] *Bubble Vision*, accessed on Oct. 2015. [Online]. Available: https://www.bubblevision.com

[36] *Hawai.i Undersea Research Laboratory*, accessed on Oct. 2015. [Online]. Available: https://www.soest.hawaii.edu/HURL

[37] *The Man Who Swims With Crocodiles*, accessed on Oct. 2015. [Online]. Available: https://www.youtube.com/watch?v=I7fZZUfvx0s

[38] *Pisces V*, accessed on Oct. 2015. [Online]. Available: http://en.wikipedia.org/wiki/Pisces_V

Yan-Tsung Peng (S'12) received the B.S. degree in computer science and engineering from Yuan Ze University, Chung-Li, Taiwan, in 2002, and the M.S. degree in computer science and information engineering from National Chiao Tung University, Hsinchu, Taiwan, in 2004. He is currently pursuing the Ph.D. degree in electrical and computer engineering from the University of California at San Diego, La Jolla.

From 2005 to 2009, he was a Senior Engineer with Novatek Microelectronics Corporation. From 2009 to 2013, he was an Assistant Patent Examiner with the Taiwan Intellectual Property Office. His research interests include image and video compression and processing.

Mr. Peng was a recipient of a Taiwan Government Scholarship for Overseas Study (Ministry of Education) in 2011.

Pamela C. Cosman (S'88–M'93–SM'00–F'08) received the B.S.(Hons.) degree in electrical engineering from the California Institute of Technology, Pasadena, CA, USA, in 1987, and the Ph.D. degree in electrical engineering from Stanford University, Stanford, CA, in 1993.

From 1993 to 1995, she was an NSF Post-Doctoral Fellow with Stanford University and a Visiting Professor with the University of Minnesota. In 1995, she joined the faculty of the Department of Electrical and Computer Engineering, University of California at San Diego, La Jolla, CA, where she is currently a Professor. Her research interests are in the areas of image and video compression and processing and wireless communications.

Dr. Cosman is a member of Tau Beta Pi and Sigma Xi. She was the Director of the Center for Wireless Communications with University of California at San Diego from 2006 to 2008, and was the Associate Dean for Students of the Jacobs School of Engineering from 2013 to 2016. She has been a member of the Technical Program Committee or the Organizing Committee for numerous conferences, including the 1998 Information Theory Workshop in San Diego, the ICIP 2008–2011, the QOMEX 2010–2012, the ICME 2011–2013, the VCIP 2010, the PacketVideo 2007–2013, the WPMC 2006, the ICISP 2003, the ACIVS 2002–2012, and the ICC 2012. She was an Associate Editor of the IEEE COMMUNICATIONS LETTERS (1998–2001), and an Associate Editor of the IEEE SIGNAL PROCESSING LETTERS (2001–2005). For the IEEE JOURNAL ON SELECTED AREAS IN COMMUNICATIONS, she served as a Guest Editor of the 2000 special issue of the IEEE JOURNAL ON SELECTED AREAS IN COMMUNICATIONS ON ERROR-resilient image and video coding, as a Senior Editor (2003–2005 and 2010–2013), and as the Editor-in-Chief (2006–2009). She received various awards including the ECE Departmental Graduate Teaching Award, the Career Award from the National Science Foundation, the Powell Faculty Fellowship, the Globecom 2008 Best Paper Award, and the HISB 2012 Best Poster Award.